# Search for Large Extra Dimensions in the Diphoton Final State at the Large Hadron Collider

by

Duong Nguyen

B.Sc., University of Natural Sciences; Ho Chi Minh City, Vietnam, 2000

M.Sc., University of Natural Sciences; Ho Chi Minh City, Vietnam, 2004

A dissertation submitted in partial fulfillment of the
requirements for the degree of Doctor of Philosophy
in The Department of Physics at Brown University

PROVIDENCE, RHODE ISLAND

May 2011

This dissertation by Duong Nguyen is accepted in its present form
by The Department of Physics as satisfying the
dissertation requirement for the degree of Doctor of Philosophy.

Date_____ _____

Professor Greg Landsberg, Advisor

Recommended to the Graduate Council

Date_____ _____

Professor Chung-I Tan, Reader

Date_____ _____

Professor David Cutts, Reader

Approved by the Graduate Council

Date_____ _____

Peter M. Weber, Dean of the Graduate School

# Acknowledgements

It is my pleasure to thank the many people who made this dissertation possible.

First of all, I would like to express my deep and sincere gratitude to my supervisor, Professor Greg Landsberg. I thank him for his great guidance, assistance, stimulating suggestions, and encouragement during these years of my research. His patience, flexibility, and belief in me have boosted my confidence to become an independent researcher.

Next, I would like to thank my Brown University's group for providing such a wonderful working environment and for being so supportive to me during these years. It was really a pleasure to be a part of the group. My special thanks to John Paul Chou for all his help, for always being kind to answer all sorts of questions and giving me valuable suggestions on my dissertation.

I am also grateful to my committee members, Professor David Cutts and Professor Chung-I Tan for spending their time to read my thesis and give me their valuable advice and suggestions.

My special thanks to Quyen Nguyen and Vietnamese friends at Brown University for their constant support and friendship.

Last but not least, to my parents and my little family, I owe the biggest debt of

gratitude. Without their unconditional love and consistent support over the years, I would never have gotten this far.

Abstract of " Search for Large Extra Dimensions in the Diphoton Final State at the Large Hadron Collider " by Duong Nguyen, Ph.D., Brown University, May 2011

We performed a search for large extra spatial dimensions via virtual graviton exchange in the diphoton channel with the Compact Muon Solenoid detector at the Large Hadron Collider. No excess of events above the Standard Model predictions has been found using a data sample collected in proton-proton collisions at the $\sqrt{s} = 7$ TeV and corresponding to an integrated luminosity of approximately 36 $\text{pb}^{-1}$. New limits are set on the effective Planck scale in the range of 1.6-2.3 TeV, at the 95% confidence level, depending on the number of extra dimensions. These are the most restrictive bounds on models with more than two large extra dimensions to date.

# Contents

# List of Tables

# List of Figures

# Chapter 1

# Introduction

For nearly forty years, the Standard Model (SM) has proven to be a very successful theory framework in particle physics. Its phenomenological predictions have been confirmed by a variety of measurements upto TeV scale at fixed target, lepton and hadron collider experiments. However, there are many unanswered questions in the theoretical construction of the SM that make us believe that the SM is an incomplete model. Furthermore, the existence of two fundamental scales that are so different from each other results in the so-called hierarchy problem. This has led to the idea of extending our 3+1 space-time dimensions to include additional compactified large extra dimensions. This dissertation presents a search for the existence of these extra dimensions at the Large Hadron Collider.

We begin this chapter with an overview about the SM and its history. After that, we describe the hierarchy problem and one of its solutions, the Large Extra Dimension paradigm. Finally, we review results from different experimental searches for large extra dimensions.

## 1.1 The Standard Model of High Energy Physics

The Standard Model of high energy physics is a relativistic quantum field theory describing the interactions between fundamental particles. There are four known types of interactions: gravitation, electromagnetic, weak and strong. The interactions act between leptons and quarks via spin-1 intermediate vector bosons. The electromagnetic and weak interactions are unified and described in a common framework called the electroweak theory.

Leptons and quarks are fermions and are organized in 3 generations. The question why there are three generation can not be answered by the Standard Model itself. The photon, W and Z bosons, and gluons are responsible for transmitting the electromagnetic, weak and strong interactions, respectively. Although the quantum treatment of gravity is incomplete, the massless spin-2 graviton is considered the gauge boson of the gravitational field and transmits the gravitational force. The gravitational attraction is very small for microscopic particles compared to other forces ($10^{-29}$ weaker than the weak force). Therefore, it is usually ignored when considering interactions between particles. However, its tiny strength raises a question about the naturalness of the theoretical construction. This is referred to the hierarchy problem of the SM.

Table 1.1 lists SM particles with six leptons and six quarks arranged in a 3-generation structure. Beside the electric charge, quarks have an additional degree of freedom called the color charge which is red ($r$), blue ($b$) or green ($g$). Note that for each particle, there is an partner anti-particle which has the same mass, but opposite electric and color charge.

The interactions between fundamental particles of the SM can be described by a

| Generation | Particle | Mass | Charge |
|---|---|---|---|
| | Leptons | | |
| 1 | Electron ($e$) | 0.5110 MeV/$c^2$ | -1 |
| 1 | Electron neutrino ($\nu_e$) | - | 0 |
| 2 | Muon ($\mu$) | 105.6 MeV/$c^2$ | -1 |
| 2 | Muon neutrino ($\nu_\mu$) | - | 0 |
| 3 | Tau ($\tau$) | 1776.90 $\pm$ 0.20 MeV/$c^2$ | -1 |
| 3 | Tau neutrino ($\nu_\tau$) | - | 0 |
| | Quarks | | |
| 1 | Up ($u$) | 1.5-3.0 MeV/$c^2$ | 2/3 |
| 1 | Down ($d$) | 3-7 MeV/$c^2$ | -1/3 |
| 2 | Charm ($c$) | 1.25 $\pm$ 0.09 GeV/$c^2$ | 2/3 |
| 2 | Strange ($s$) | 95 $\pm$ 0.25 MeV/$c^2$ | -1/3 |
| 3 | Top ($t$) | 172.5 $\pm$ 2.7 GeV/$c^2$ | 2/3 |
| 3 | Bottom ($b$) | 4.20 $\pm$ 0.07 GeV/$c^2$ | -1/3 |

**Table 1.1:** Standard Model particles [1].

Lagrangian. In order to satisfy that the theory to be renormalizable, the Lagrangian is required to be invariant under local gauge transformations. The local gauge transformation belongs to a gauge symmetry group. The SM dynamical properties are described by the $SU(3)_C \otimes SU(2)_L \otimes U(1)_Y$ gauge group structure, where C denotes the color charge, L implies that SU(2) acts on the left-handed components and Y is the weak hypercharge which relates to electric charge Q and the third component of the weak isospin $I_3$ by the equation, $Y = 2(Q - I_3)$. The electroweak interaction is described by the $SU(2)_L \otimes U(1)_Y$ sector while the strong interaction is described by the $SU(3)$ gauge transformation group.

The local gauge invariant requirement on the Lagrangian introduces new fields and their associated spin-1 gauge bosons. For the SU(2) gauge transformation, the gauge fields are $W^i_\mu$, i = 1,..,3. The gauge field corresponding to the U(1) transformation is $B_\mu$. The $W^{1,2}_\mu$ gauge fields are combined to form the charge states

$W_\mu^+$, $W_\mu^-$, which are identified as the physical $W^\pm$ bosons, according to

$$W_\mu^\pm = \frac{-W_\mu^1 \pm iW_\mu^2}{\sqrt{2}} \tag{1.1}$$

$$W_\mu^0 = W_\mu^3 \tag{1.2}$$

The unification of the electromagnetic and weak interactions following the $SU(2) \otimes U(1)$ gauge group is expressed in the combination of $B_\mu$ and $W_\mu^3$:

$$A_\mu = \frac{g_2 B_\mu - g_1 Y_L W_\mu^3}{\sqrt{g_2^2 + g_1^2 Y_L^2}} \tag{1.3}$$

$$Z_\mu = \frac{g_1 Y_L B_\mu + g_2 W_\mu^3}{\sqrt{g_2^2 + g_1^2 Y_L^2}} \tag{1.4}$$

where $Y_L$ is the left-handed projection of the hypercharge Y, for which $Y_L = -1$, $g_1$ and $g_2$ are the coupling constants of the U(1) and SU(2) fields, $A_\mu$ and $Z_\mu$ correspond to massless photon and neutral boson Z, respectively. Defining $sin\theta_w = g_1/\sqrt{g_1^2 + g_2^2}$, where $\theta_w$ is the Weinberg angle ($sin^2\theta_w \sim 0.23$), we have:

$$g_1 = \frac{e}{cos\theta_w} \qquad g_2 = \frac{e}{sin\theta_w} \qquad g_Z = \frac{e}{sin\theta_w cos\theta_w} \tag{1.5}$$

$$A_\mu = W_\mu^3 sin\theta_w - B_\mu cos\theta_w \quad Z_\mu = W_\mu^3 cos\theta_w + B_\mu sin\theta_w \tag{1.6}$$

where $e$ is the electromagnetic coupling constant or the electric charge, and $g_Z$ is the coupling constant of $Z_\mu$ field.

Local gauge invariant requires the bosons to be massless. However, experiment measurements exclude this for the W and Z bosons. Therefore, the symmetry is not exact, but it is spontaneous broken by the Higgs mechanism to give mass to the gauges bosons. At the leading order, the SM predicts that $M_W/M_Z = cos\theta_w$.

Quarks and leptons are arranged into left-handed doublets and right-handed

singlets. For example, the first generation lepton doublet is ($\nu_{eL}$, $e_L$) and the singlet is $e_R$. For leptons, the charge current weak interaction transmitted by $W^{\pm}$ gives strictly transitions within a generation. For quark doublets, generational mixing occurs for example ($u_L$, $d_L^{'}$), $d_L^{'} = d_L cos\theta_C + s_L sin\theta_C$. Therefore, the charge-changing transition happens between generations. The neutral- current interaction is transmitted by the Z boson without charge changing. This interaction transmutes the doublet and the singlet members into themselves.

The SU(3) group of local gauge transformation, which changes the color, has eight generators corresponding to eight $G_{\mu}^{a}$ fields (a=1,...,8). Therefore, there are eight massless gauge bosons carrying pair of color labels, called the gluons. The strength of strong interaction varies with distances. It is weak at short distances but strong at large distances. This feature is called asymptotic freedom and it is explained why quarks are confined inside hadrons. Furthermore, since gluons carry color, they couple directly to each other. Therefore, calculations in quantum chromodynamic (QCD) theory are very challenging. Table 1.2 summarizes the gauge boson of the SM.

| Particle | Interaction | Mass (GeV/$c^2$) | Charge (e) |
|---|---|---|---|
| Photon ($\gamma$) | Electromagnetic | 0 | 0 |
| $W^{\pm}$ | Weak | 80.2 | $\pm$1 |
| Z | Weak | 91.2 | 0 |

**Table 1.2:** SM gauge bosons.

The SM was developed in 1960s and the early 1970s. Sheldon Glashow proposed the unification of the electromagnetic and the weak forces in 1963 [18]. The Higgs mechanism was incorporated in the electroweak model in 1967 by Steven Weinberg [19] and Abdus Salam [20]. Gerard 't Hooft showed that gauge theories are renormalizable in 1971 [21]. The QCD theory was completed by David Gross,

Frank Wilczek and David Politzer with the discovery of the asymptotic freedom in 1973 [22, 23]. In the same year, Kobayashi and Maskawa proposed three generation structure of the SM. However, the missing members of the third generation was observed recently in 1995 for top quark [24, 25] and in 2001 for tau neutrino [26].

## 1.2 Hard Scattering Cross Section

The LHC is a proton-proton collider. The proton quantum numbers suggest that protons are the bound state of *uud* valance quarks. They are also composed of radiated gluons and a sea of quark-antiquark pairs. These constitutions are called partons. Because the QCD coupling runs with the momentum transfer, or energy, scale of the parton-parton ($Q$) interaction and it is strong at low Q, the perturbation calculation at low Q is invalid. In general, the coupling constant is determined by the $\beta$-function. If one limits the QCD perturbative expansion of this function at the lowest order coefficient, the coupling constant $\alpha_s(Q^2)$ is defined as [**?**]:

$$\alpha_S(Q^2) = \frac{\alpha_S(\mu^2)}{1 + \frac{33-2n_f}{12\pi}\alpha_S(\mu^2) ln(Q^2/\mu^2)} \tag{1.7}$$

Where $\mu$ is the renormalization scale at which a subtraction is performed to remove the ultraviolet divergences in the renormalization procedure. This parameter is chosen arbitrarily. A convenient choice is $\mu = M_Z$ which is large enough to be in the perturbative domain. Ref. [27] quotes:

$$\alpha_s(M_Z^2) = 0.1184 \pm 0.0007 \tag{1.8}$$

Historically, a dimensionful parameter $\Lambda_{QCD} \sim 200$ MeV is introduced directly to the definition of $\alpha_S(Q^2)$. This is the value where the coupling would diverge. However,

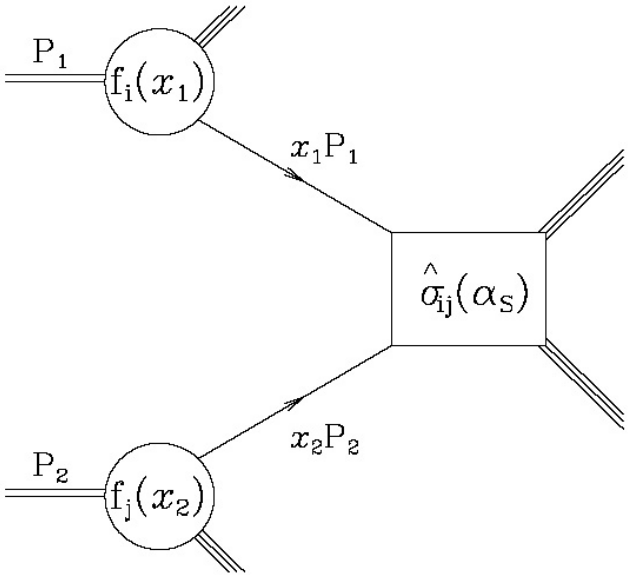


**Figure 1.1:** The parton model description of a hard scattering process [4].

this choice has some disadvantages: it is not dimensionless, depends on the number of active flavours, $n_f$, and on the renormaliztion scheme.

In hard scattering or high Q processes, the cross sections are factorized based on the factorization theorem of QCD [28]:

$$\sigma(P_1, P_2) = \sum i, j \int dx_1 dx_2 f_i(x_1, \mu_F^2) f_j(x_2, \mu_F^2) \widehat{\sigma}_{ij}(p_1, p_2, \alpha_S(\mu_R^2), Q^2/\mu_F^2) \quad (1.9)$$

where $P_1$, $P_2$ is the four-momenta of incoming hadrons, $p_1 = x_1 P_1$, $p_2 = x_2 P_2$ are the four-momentum of partons participating in the hard interaction, $f_{i,j}(x, \mu_F^2)$ are the parton (gluon or quark) distribution function (PDF) defined at a factorization scale $\mu_F$, and $\widehat{\sigma}_{ij}$ is the short-distance cross section for the scattering of the partons i and j. Because the coupling constant is small at high energy, this cross section is calculated as a perturbation series of the running coupling $\alpha_S$.

The factorization factor is an arbitrary parameter which separates the long- and

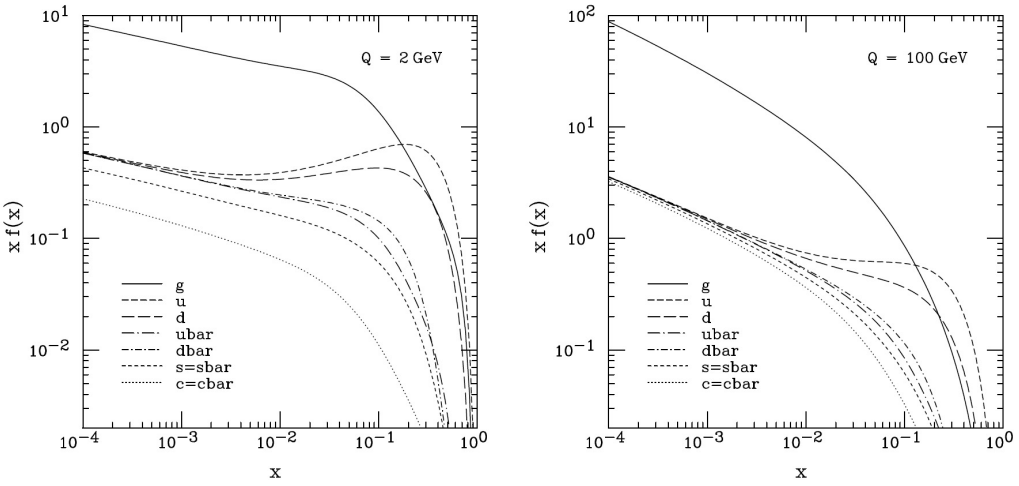


**Figure 1.2:** The CTEQ6M parton distribution functions at $Q = 2$ and 100 GeV [5].

short-distance calculation. If a emitted parton has transverse momentum less than $\mu_F$, it is considered as a part of the hadron structure and is absorbed into the parton distribution function. In contrast, a high transverse momentum parton is a part of the short-distance cross section. The dependence of cross section on $\mu_F$ is weaker if more terms are included in the perturbative expansion.

The PDFs are the probability density to find a parton inside of the proton with a given fraction of the total momentum. It is determined from experimental measurements. An example of these functions are calculated by CTEQ collaboration based on QCD studies at HERA and the Tevatron. Both the parton distribution functions and short-distance cross section, $\widehat{\sigma}$, depend on the scales. Therefore, the scales need to be used consistently in the PDF and the short-distance calculation. Otherwise, cancellation of ultraviolet and collinear divergences do not meet. A common setup for scales is $Q^2 = \mu_R^2 = \mu_F^2$.

## 1.3 The Direct Photon Production

Direct photons are photons produced in the parton-parton collisions, which distinguish to photons from decays of neutral hadrons (for example $\pi_0$). A photon is created in association with jets in the Compton process ($qg \rightarrow \gamma q$) or annihilation process ($q\overline{q} \rightarrow \gamma q$) (see Figure 1.3). These are leading order perturbation contributions in the cross section calculation (O($\alpha\alpha_S$), $\alpha$ and $\alpha_S$ are the electromagnetic and strong couplings, respectively).

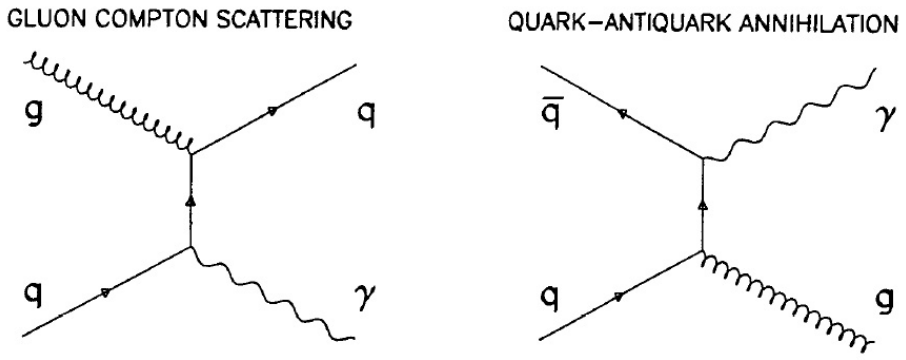


**Figure 1.3:** Leading order Feynman diagram of gamma+jet process.

Photon pairs are also produced in proton-proton collisions. The LO cross section (O($\alpha^2$)) comes from the quark-antiquark annihilation ($q\overline{q} \rightarrow \gamma\gamma$). The diagram is called the Born diagram (diagram a in Figure 1.4). Diagrams d and g in Figure 1.5 show the one and two fragment processes where one or both photons come from the collinear fragmentation of hadrons. These diagrams are also at LO. The next-to-leading order diagrams include real (diagram b in Figure 1.5) or virtual (diagram c in Figure 1.5) corrections, which are O($\alpha_S$), to the LO Born diagram. Therefore, the total NLO contribution is O($\alpha_2\alpha_S$). The corresponding NLO fragmentation processes are shown in Figure 1.5, diagrams e, f, h, i.

There are multi collinear singularities in the fragmentation diagrams when a

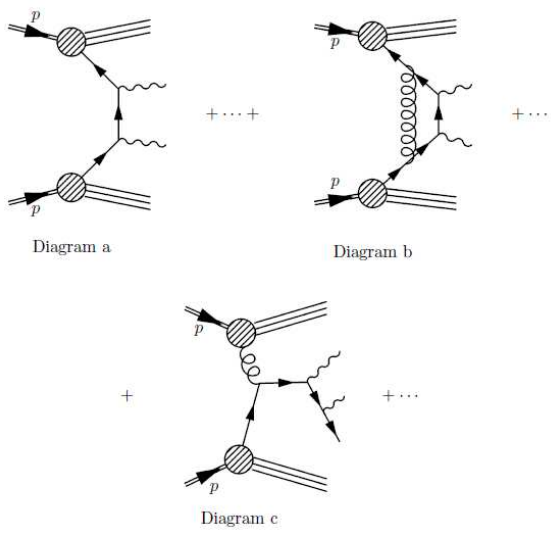


**Figure 1.4:** The direct contributions to the diphoton cross section. Diagram a: the LO Born process. Diagram b and c: the NLO processes

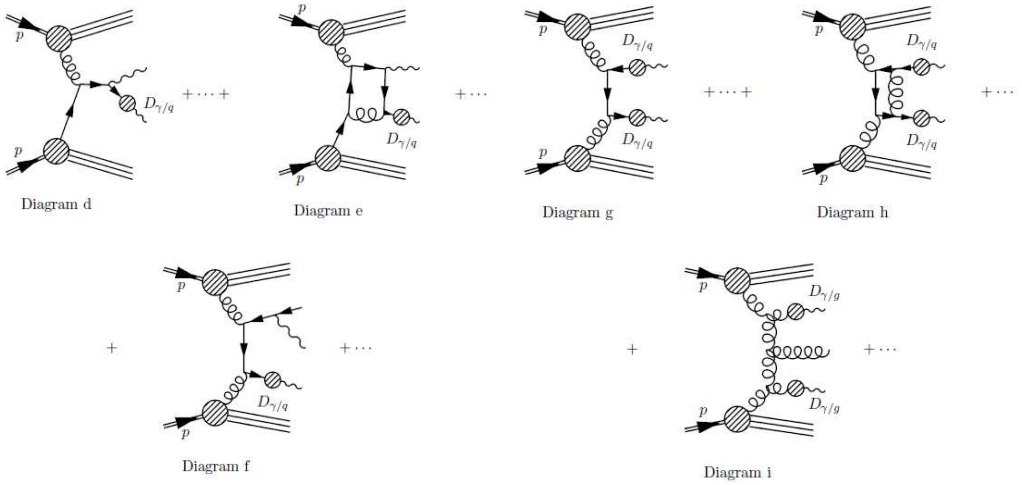


**Figure 1.5:** The fragmentation contributions to the diphoton cross section. Diagrams d and g: the LO processes. Diagrams e, f, h, i: the corresponding NLO processes. $D_{\gamma/qorg}$ is the fragmentation function which absorbs the quark-photon singularity

high $p_T$ parton undergoes a cascade of successive collinear splittings ending up with a parton-photon collinear splitting (momenta of photon and parton are nearly parallel). These singularities are absorbed into a photon "fragmentation function" $D_{\gamma/q,g}(z,\mu^2)$ representing the probability of finding a photon carrying a longitudinal momentum fraction z in a quark or gluon jet at a scale $\mu$. If this scale, often chosen at the order of the hard scale of the process, is large compared to any typical hadronic scale

($\sim$ 1 GeV), these functions have a size of roughly $\alpha/\alpha_S(\mu)$. Therefore, they compensate the strong interaction vertex contribution, which is $O(\alpha_S)$, in cross section calculation.

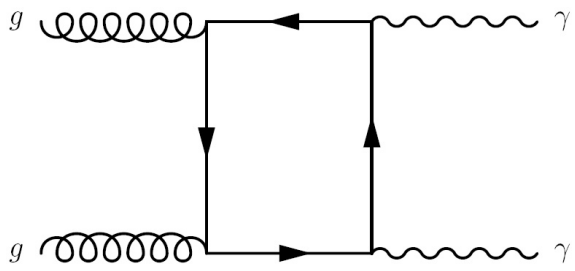


**Figure 1.6:** The box diagram

Finally, the gluon-gluon fusion process or box diagram is at the NNLO (next-to-next-to-leading order) level suppressed by $O(\alpha_S^2)$. However, it is often included in the calculations of the xs at the LHC due to the high gluon luminosity.

## 1.4 The Hierarchy Problem and Large Extra Dimensions Paradigm

The hierarchy problem refers to the enormous difference between the electroweak symmetry breaking scale, $M_{EWSB} \sim 10^3$ GeV, and the fundamental scale of gravity, $M_{Pl} \sim 10^{19}$ GeV. The consequence of this large difference in scale is that a very high degree of fine-tuning is required to protect the Higgs mass from radiative corrections. For example, the correction for Higgs mass from fermi loops (Figure 1.7) is given by:

$$\Delta M_H^2 = \frac{\lambda_f^2}{4\pi^2}(\Lambda^2 + M_H^2) + ... \tag{1.10}$$

where $\Lambda$ is the ultraviolet cutoff and $\lambda_f$ is the self coupling constant of the Higgs bosons. If $\Lambda$ is at the order of $M_{Pl}$, the constraint of Higgs mass at ∼100 GeV requires the fine tuning or cancellation of various loops to a precision of $\sim (M_H/\Lambda)^2 \sim 10^{-34}$.

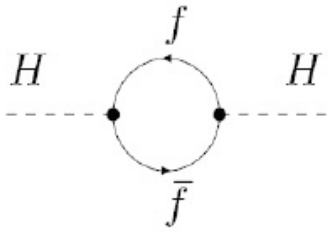


**Figure 1.7:** The fermion loop correction to Higgs mass

In 1998, Arkani-Hamed, Dimopoulos and Dvali (ADD) proposed the Large Extra Dimensions paradigm to solve the hierarchy problem [29]. In this framework, the SM particles and gauge interactions are constrained to the common 3 + 1 space-time dimensions, while gravity is free to propagate through the entire multidimensional space (bulk). Therefore, the gravitational force is effectively diluted, and it appears to be weak (strength order $\sim 1/M_{Pl}$) for an observer in the SM brane. For instance, suppose that there are n extra compact spatial dimensions of the same radius ∼R. By applying the Gauss's law in (4+n) dimensions, the gravitational potential between two test masses, $m_1$, $m_2$ separated by a distance of $r \ll R$ is[29]

$$V(r) \sim \frac{m_1 \times m_2}{M_D^{n+2}} \frac{1}{r^{n+1}}, (r \ll R) \tag{1.11}$$

where $M_D$ is the fundamental Plank scale of a (4+n) dimensional theory. If two masses are separated by $r \ll R$, their gravitational flux lines can not continue to penetrate in the extra dimensions. Therefore, the potential is:

$$V(r) \sim \frac{m_1 \times m_2}{M_D^{n+2} R^n} \frac{1}{r}, (r \gg R) \tag{1.12}$$

Compared to the Newtonian gravitational potential, our effective $M_{Pl}$ is:

$$M_{Pl}^2 \sim M_D^{n+2} R^n \tag{1.13}$$

If we set $M_D \sim M_{EW} \sim 1$ TeV, we find that

$$R \sim 10^{\frac{30}{n_{\rm ED}} - 19} \text{m}. \tag{1.14}$$

$n_{ED} = 1$ case is excluded because $R$ is approximately $10^{11}$ m which is on the order of the radius of the Solar system. For $n_{ED} = 2$, $R < 10^{-2}$ cm, which is out of the reach of direct measurements of gravity at short distances[30] (as of 1998, gravitational measurements are not sensible to the distance smaller than 1 mm). For $n_{ED} = 6$ or 7 (corresponding to the 10 or 11-dimension space-time suggested by the string theory), the size of the extra dimensions is $\sim 1$ fm, which is fairly large compared to Plank or electroweak lengths; hence, the name Large Extra Dimensions.

An enhancement of the gravitation in the case of extra dimensions can be explained in a manner similar to the "particle-in-box" problem. Because gravitons propagate in the compact extra dimensions, the boundary conditions result in a quantization of the graviton's energy into discrete eigenvalues. From the point of view of a 3-dimensional observer, they look like a tower of graviton excitations, referred to Kaluza-Klein modes. Since the energy spacing between modes is very small ($\sim 1 - 100meV$ given the size of EDs $\sim 10^{-3} - 10^{-15}$ m), there are many KK modes to be excited at high energy. Although each KK mode couples to the energy-momentum tensor with the gravitational strength $G_N \sim 1/M_{Pl}^2$, the large number of these modes is sufficient to enhance the gravitational coupling tremendously. For example, at the energy of 1 TeV, given the size of ED $\sim 1$ fm and $n_{ED}$ =7, as many as $10^{28}$ modes can be excited [31].

The requirement that all particles except gravitons are constrained to the SM brane and must not feel the extra space satisfies constraints from atomic physics and other experimental data. Although the ADD paradigm solves the hierarchy problem by suggesting a fundamental Plank scale of the order of EW scale in the multidimensional space, it converts the energy hierarchy to a distance hierarchy since the size of the extra dimensional space is much larger than the range of EWSB energy scale (about $10^{-19}$ m). With the existence of extra dimensions, the electroweak scale is the only fundamental scale in nature where the gravitational and gauge interactions unite. Thus, the Plank scale is not the fundamental scale, but its enormity is due to the large size of the new dimensions.

## 1.5 Searches for Large Extra Dimensions at Colliders

The production of KK gravitons ($G_{KK}$) at colliders is possible since gravitons couple to the energy-momentum tensor. This implies that graviton can be added to any vertices or lines of SM Feynman diagrams. One can look for the graviton emission which results in a single jet or a gauge boson associated with a large missing transverse energy due to escapes of gravitons to the extra dimension space. Direct graviton emissions depend directly to the fundamental Plank scale $M_D$. However, it is expected to be suppressed by a factor $(\sqrt{\hat{s}}/M_D)^{n_{\mathrm{ED}}+2}$, where $\sqrt{\hat{s}}$ is the characteristic center-of-mass energy at which the effects of EDs are most pronounced. Furthermore, the dependence on the number of extra dimensions for the virtual graviton effects is fairly weak [32, 33]. An other channel to look for ED effect is the virtual graviton production via Drell-Yan like processes. Subsequently, gravitons decay to

two photons or fermions. The later is less sensitive because decays of spin 2 gravitons to spin 1/2 fermions is suppressed in the s-wave mode. The virtual graviton channel is a complement to the direct graviton emission channel because it depends on the ultra violet cutoff $M_S$ of the KK spectrum. $M_S$ is general lower than $M_D$, so the extra dimension effect might be firstly seen in the virtual graviton channel.

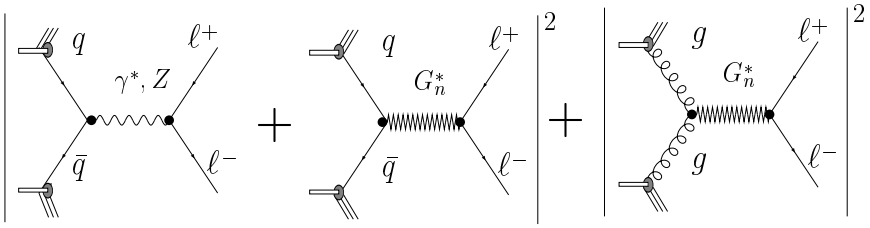


**Figure 1.8:** DY production Feynman diagrams including the large extra dimensions [6].

The virtual graviton exchange diagrams interfere with their SM counterparts as shown in Figure 1.8 for the DY production. The consequence of additional contributions from these diagrams is an enhancement in DY or diboson spectrum at high invariant masses. The cross section of virtual graviton exchange is not well-defined since it depends on a particular representation of the interaction Lagrangian and the definition of the ultraviolet cutoff on the KK modes. There are three such representations [32, 33, 34]. All of them use a variable $\eta_G = \mathcal{F}/M_S^4$, where $\mathcal{F}$ is a dimensionless parameter, and $M_S$ is the ultraviolet cutoff, to parameterize the total or differential cross section with contribution from the $G_{KK}$ exchange:

$$\sigma_{\text{tot}} = \sigma_{\text{SM}} + \eta_G \sigma_{\text{int}} + \eta_G^2 \sigma_G, \tag{1.15}$$

where $\sigma_{\text{SM}}$ is the SM cross section, $\sigma_{\text{int}}$ is the interference term and $\sigma_G$ is the pure gravitational effect term.

The parameter $\mathcal{F}$ contain the dependence of virtual $G_{KK}$ exchange effect on the number of extra dimensions. These are its definitions used in each representation

mentioned above:

$$\mathcal{F} = 1, \text{ (GRW [32])}; \tag{1.16}$$

$$\mathcal{F} = \begin{cases} \log\left(\frac{M_S^2}{M^2}\right), & n = 2 \\ \frac{2}{n-2}, & n > 2 \end{cases}, \text{ (HLZ [34])}; \tag{1.17}$$

$$\mathcal{F} = \frac{2\lambda}{\pi} = \pm\frac{2}{\pi}, \text{ (Hewett [33])}. \tag{1.18}$$

In the above formula, $\mathcal{F}$ depends explicitly on the number of EDs only in the HLZ formalism. The gravity effect contributes constructively in both HLZ and GRW formalism. However, the sign of $\mathcal{F}$ is unknown and included in a parameter $\lambda$ in Hewett convention. $\lambda$ is of order 1 and usually assigned either $+1$ (constructive interference) or $-1$ (destructive interference).

## 1.6 Current Constraints and Limits

Search for extra dimensions have been performed by many experiments and the model parameters are also constrained by astrophysical observations and cosmology. One of the most straightforward approaches is to measure the gravity directly at short distances and look for modification of Newton's gravitational law. This modification is parameterized by the Yukawa potential.

$$V(r) = -G\frac{m_1 m_2}{r}\left(1 + \alpha e^{-r/\lambda}\right) \tag{1.19}$$

These measurements are sensitive to distances $\sim 50\mu$m with the current techniques. If all extra dimensions have the same sizes, this limit implies that these measurements can not go beyond $n = 2$ case. However, only the total volume of extra dimensions

is necessary, not the shape of extra dimensions. Therefore, one of extra dimensions might be macroscopic and sensitive to direct measurements probing $n > 2$ cases. The best limit on the size of extra dimensions is given by Eöt-Washington group [35], which is $R < 0.44\ \mu m$ at 95% CL. This limit corresponds to $M_D > 3.2$ TeV for two extra dimensions of equal sizes [7].

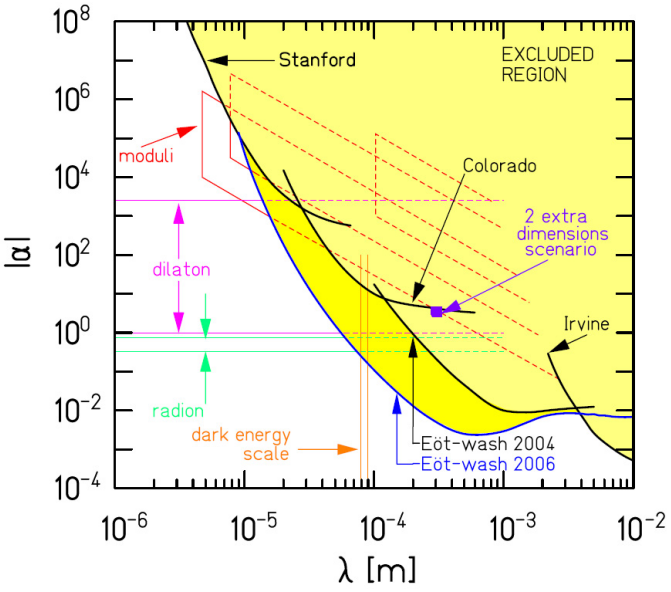


**Figure 1.9:** Constraints on Yukawa violations of the gravitational $1/r^2$ law. The shaded region is excluded at the 95% confidence level [7].

An example of constraining ADD model using astrophysical observations comes from the observation of a handful of neutrinos from SN1987A explosion by IMB and Kamiokande detectors. This method is based on the assumption that KK graviton emission is an competitive cooling mechanism for the supernovae; thus the dominant SM mechanism, the neutrino emission is suppressed. The constraints on $M_D$ found are $M_D > 25 - 30$ GeV for $n = 2$ and 2-4 TeV for $n = 3$ and below 1 TeV for any higher number of extra dimensions [36]. In general, the limits from astrophysical observation and cosmology are strong (up to 1700 TeV) for $n = 2$, moderate (few TeV) for $n = 3$, and rather weak for $n > 3$ [31]. The uncertainties in predictions are

**Table 1.3:** 95% CL lower limits on the fundamental Planck scale $M_D$ (in TeV) form Tevatron experiments [2].

| Experiment and channel | $n = 2$ | $n = 3$ | $n = 4$ | $n = 5$ | $n = 6$ |
|---|---|---|---|---|---|
| LEP Combined | 1.60 | 1.20 | 0.94 | 0.77 | 0.66 |
| CDF monophotons, 2.0 fb$^{-1}$ | 1.08 | 1.00 | 0.97 | 0.93 | 0.90 |
| DØ monophotons, 2.7 fb$^{-1}$ | 0.97 | 0.90 | 0.87 | 0.85 | 0.83 |
| CDF monojets, 1.1 fb$^{-1}$ | 1.31 | 1.08 | 0.98 | 0.91 | 0.88 |
| CDF combined | 1.42 | 1.16 | 1.06 | 0.99 | 0.95 |

**Table 1.4:** Recent 95% CL lower limits on the ultraviolet cutoff $M_S$ (in TeV) from the Tevatron experiments [2].

| DØ Signature | GRW | HLZ | | | | |
|---|---|---|---|---|---|---|
| | | $n$=2 | $n$=3 | $n$=4 | $n$=5 | $n$=6 | $n$=7 |
| $ee + \gamma\gamma$, 1.1 fb$^{-1}$ | 1.62 | 2.09 | 1.94 | 1.62 | 1.46 | 1.36 | 1.29 |
| Dijets, 0.7 fb$^{-1}$ | 1.56 | | 1.85 | 1.56 | 1.41 | 1.31 | 1.24 |

large due to high uncertainties of the astrophysical measurements.

At colliders, LEP experiments searched for extra dimension in both direct graviton emission channel via $e^+e^- \rightarrow \gamma/Z + G_{\rm KK}$ and virtual graviton production via fermions or diboson channels. However, the $e^+e^- \rightarrow \gamma + G_{\rm KK}$ and the $e^+e^- \rightarrow e^+e^-/\gamma\gamma$ channels are the most sensitive. D0 and CDF collaboration also searched for gravitational effect in virtual graviton production, monojet and monophotons channels. The most recent 95% limits using 1-3 fb$^{-1}$ data from those searches are presented in Table 1.4. CDF gives the most stringent limits on $M_D$ in the combined monojet and monophoton channel. The best $M_S$ limits comes from D0 using the combined $ee + \gamma\gamma$ channel. D0 also performed for the first time the search in the dijet channel.

# Chapter 2

# Experimental Apparatus

The Large Hadron Collider (LHC) is the highest energy hadron collider to date, which collides proton-proton beams at the designed center of mass energy of 14 TeV. In 2010, when the analysis presented in this dissertation, was carried out, the center-of-mass energy of the proton-proton collisions is 7 TeV. The Compact Muon Solenoid (CMS) detector, located at Point 5, measures the outcomes of the collisions. The data collected by CMS are used in a search for large extra dimensions presented in this dissertation. The LHC accelerator complex and the CMS detector are described in Section 2.1 and Section 2.2, respectively.

## 2.1 The Large Hadron Collider

The Large Hadron Collider (LHC) is a hadron accelerator complex located at the European Organization for Nuclear Research (CERN), Switzerland [3, 8]. It is designed to accelerate proton or heavy ion beams using two main circular acceleration rings

with a circumference of 27 km inside the LEP (Large Electron Positron) tunnel. In order to reach the design collision center-of-mass energy, 14 TeV, the proton beams are accelerated through subsequent steps as shown in Figure 2.1 (left). The proton beams are injected to the Proton Synchrotron (PS) from the linear accelerator and accelerated to 25 GeV before being injected to the Super Proton Synchrotron (SPS). The SPS raises their energy to 450 GeV. Finally, the beams are injected to the main LHC rings and circulate in opposite directions until reaching the nominal energy. The beams collide at 4 interaction points where the ALICE (An LHC Heavy Ion Experiment), ATLAS (A Toroidal LHC Apparatus), CMS (Compact Muon Solenoid), and LHCb (LHC beauty experiment) experiments are located. Figure 2.1 (right) shows the basic layout of the LHC main ring which has eight arcs and eight straight sections (about 528 m long each). The experiments are located at the straight sections. ATLAS and CMS are the two high-luminosity experiments located at Point 1 and Point 5, respectively.

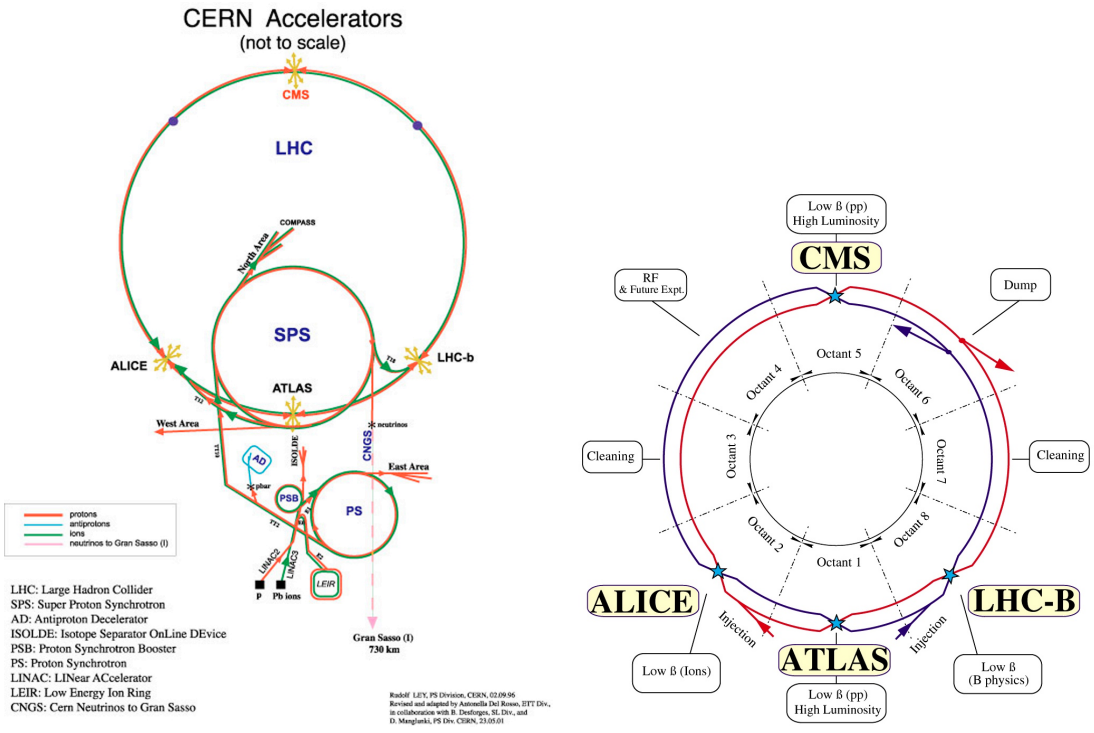


**Figure 2.1:** The LHC accelerator complex (left) and the main ring layout (right)

At design, the beams are packed in a large number of closely spaced bunches, 3564 in total along the LHC orbit, and separated in time by 25 ns (approximately 7.5 m). However, only 2835 bunches are used for collisions with detailed structure decided by the injection scheme and the properties of the dump system. The beams cross each other by a small angle at the interaction points (200 $\mu$rad) in order to avoid unwanted collisions [3]. The luminosity is given by:

$$L = \frac{N^2 k_b \gamma}{4\pi \epsilon_n \beta^*} F, \tag{2.1}$$

where N is the number of protons per bunch, $k_b$ is the number of bunches, f is the revolution frequency, $\gamma$ is the relativistic factor, $\epsilon_n$ is the normalized transverse emittance, $\beta^*$ is the beta function value at the interaction point, and F is the reduction factor caused by the crossing angle ($\sim$0.9 at the LHC). Table 2.1 lists the nominal values of those parameters for the design instantaneous luminosity L = $10^{34}$ cm$^{-2}$s$^{-1}$.

| N | $k_b$ | f | $\epsilon_n$ | $\beta^*$ |
|---|---|---|---|---|
| 1.15$\times 10^{11}$ | 2835 | 400 MHz | 3.75 $\mu$m.rad | 0.5 m |

**Table 2.1:** LHC designed parameters[3]

The LHC NbTi superconducting magnets are designed to maintain an 8 T field. They are cooled by superfluid helium at a temperature below 2 K. The main part of the LHC rings contains 1232 two-in-one dipoles. As shown in Figure 2.2, two beams are kept in separated dipoles in the same cryostat. There are also quadrupole and multipole magnets to focus and stabilize the beams, respectively.

The first collisions at the LHC took place in November 2009 with an energy of 450 GeV per beam. The energy increased to 1.18 TeV per beam in December 2009 and later to 3.5 TeV in March 2010 which was maintained during 2010 run. The

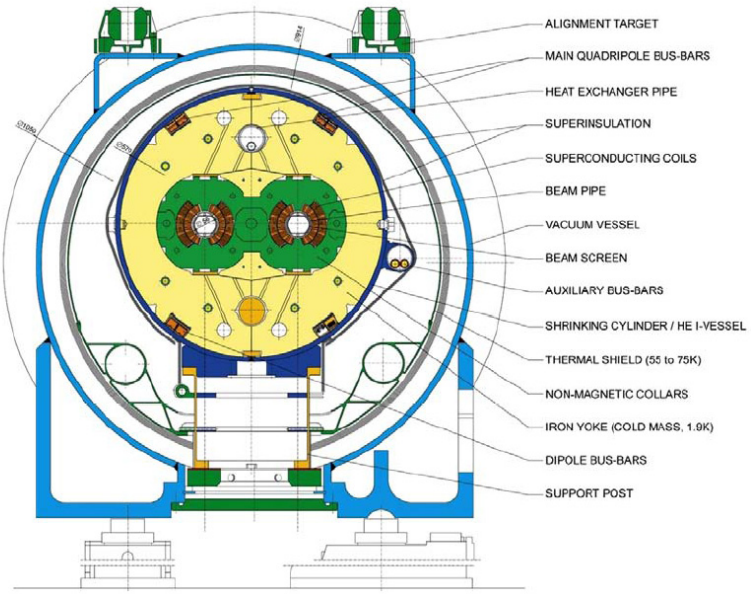


**Figure 2.2:** Cross section of a LHC diplole [8].

LHC will continue running at this energy in 2011. The instantaneous luminosity increased from $10^{27}$ cm$^{-2}$s$^{-1}$ in March 2010 to its peak, $2\times10^{32}$ cm$^{-2}$s$^{-1}$ in October 2010. Figure 2.3 shows the integrated luminosity evolution of LHC in 2010. The integrated luminosity increased steeply toward the end of the run, and the LHC delivered a total of 47 pb$^{-1}$ of collision data in 2010.

## 2.2 The CMS Detector

### 2.2.1 Overview

CMS uses a right-handed coordinate system, where the $x$-axis points radially inward toward the center of the LHC, the $y$-axis points vertically upward, and the $z$-axis points along the counter-clockwise beam direction (toward the Jura mountains from the LHC Point 5). We measure the polar angle $\theta$ with respect to the $z$-axis and define

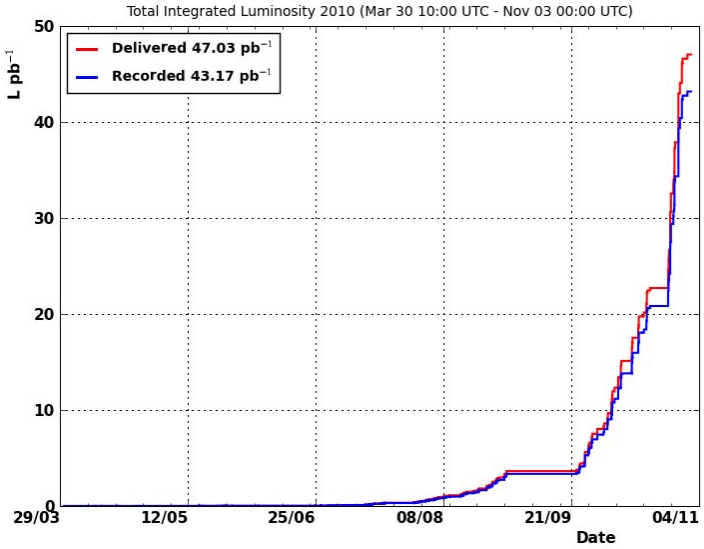


**Figure 2.3:** The integrated luminosity evolution in 2010 at CMS.

the pseudorapidity $\eta \equiv -\ln\tan(\theta/2)$. The azimuthal angle, $\phi$, is measured with respect to the $x$-axis. The transverse quantities, for example transverse momentum or energy, are measured in the plane transverse to the beam direction. Thus, they are calculated from the $x$ and $y$ components.

The CMS detector is a multi-purpose detector designed to perform a wide range of high-energy collider physics at the LHC [37]. It is 21.6 m long, 14.6 m in diameter, and the total weight of 12500 t. It is located in the collision hall about 100 m underground at Point 5. Despite its huge size, the design of the CMS detector is compact compared to the ATLAS detector, with all subdetectors closely installed about a large-bore superconducting solenoid. The superconducting solenoid operates at 3.8 Tesla providing large bending power ($\sim$ 12 Tm). It is 13m long, and 6 m in diameter which is large enough to contain the tracker and calorimeter systems.

The innermost subdetector is the all-silicon pixel detector whose purpose is to identify hits for track reconstruction. The 10-layer silicon microstrip detector, which

has a cylindrical shape of 5.8 m length and 2.6 m diameter is placed between the pixel detector and the electromagnetic calorimeter. The electromagnetic calorimeter (ECAL) covers up to $|\eta| \leq 3$ and is made of lead-tungstate scintillating crystals with the a thickness of 25 radiation lengths. The CMS hadronic calorimeter (HCAL) is placed after the ECAL with coverage up to $|\eta| \leq 5$. Finally, there are 4 muon stations installed outside the solenoid in the steel return yoke.This ensures robust muon track reconstruction and geometric coverage up to $|\eta| < 3$.

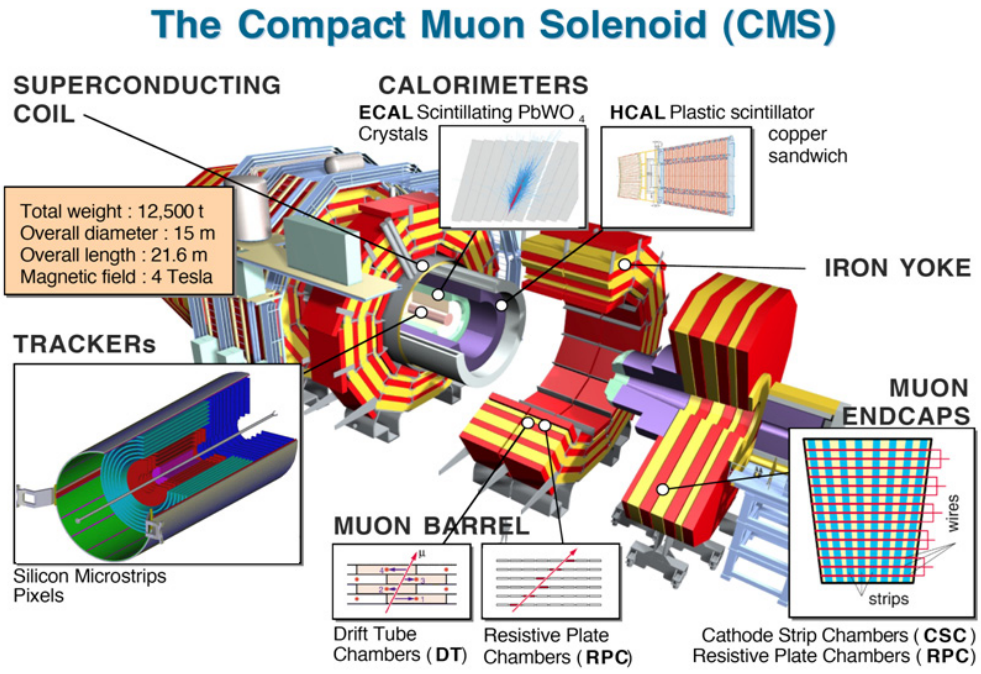


**Figure 2.4:** An overview of the CMS detector.

## 2.2.2 The Tracker

The LHC produces about 1000 particles traversing the tracker for every bunch crossing ($\sim$ 25 ns interval) at peak luminosity [37]. This requires a high- granularity and fast-response tracker to reliably reconstruct particle trajectories and vertices. Be-

cause of this, the CMS tracker is constructed entirely with silicon technology. The total active silicon area of CMS tracker is 200 $m^2$ and is composed of 1440 pixel and 15148 strip modules [37]. Figure 2.5 shows the layout of the CMS tracker. The maximum coverage of the tracker is $|\eta| \leq 2.5$. The pixel detector has 3 layers in the

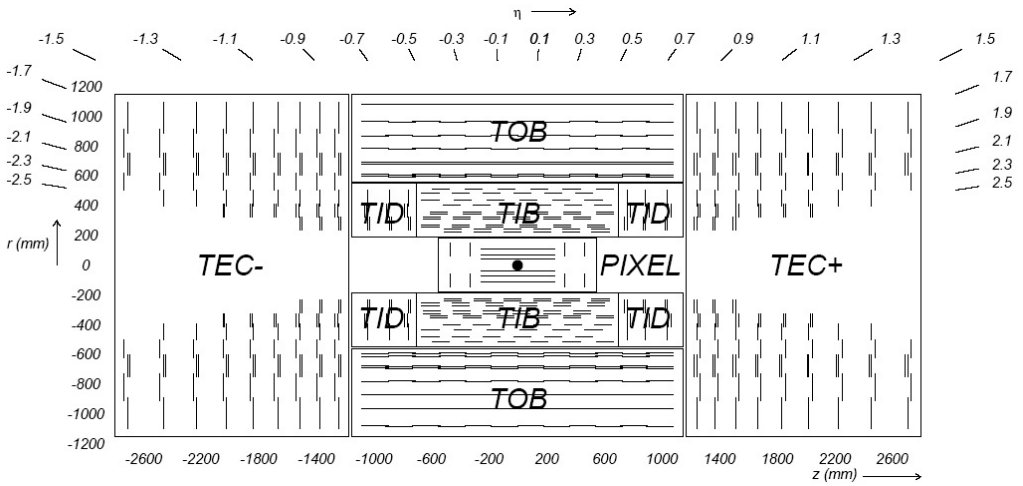


**Figure 2.5:** The tracker geometry.

barrel located between 4.4, 7.3 and 10.3 cm from the center of the detector. Each detector is 53 cm long. At the endcap, it is enclosed by 2 hollow disks with a radius of 6 and 15 cm. The inner and outer disks are at $|z|$=34.5 cm and $|z|$ =46.5 cm, respectively. There are about 66 million hybrid pixel cells in an approximately 100×150 $\mu$m square shape. Because of the high density of those small elements, the spatial resolution is approximate 10 $\mu$m in the r$-\phi$ plane and 20 $\mu$ m in the z direction.

The pixel detector is surrounded by the silicon-strip detector. In the barrel, it includes the Tracker Inner Barrel (TIB) and the Tracker Outer Barrel (TOB). The TIB has 4 layers with a half length of 65 cm and the TOB has 10 layers covering 110 cm in z at each side ($|z| < 220$ cm). The end cap region is covered by the Tracker End Cap (TEC) and the Tracker Inner Disks (TID). The 3-disk TID are embedded between the TIB and TEC. Each TEC is composed of 9 disks and extends the

longitudinal coverage from $|z|$=120 cm to $|z|$ =280 cm.

The silicon-strip detector is built from 15148 modules of 24244 sensors with 9.3 million strips. Depending on where the module is mounted, the strip pitch ranges from 80 to 180 $\mu$m. Some of the layers and rings (layers 1 and 2 for TIB and TOB; rings 1 and 2 for TID; rings 1, 2 and 5 for TECs) use a double-sided configuration in which two micro-strip detector modules are mounted back-to-back with a stereo angle of 100 mrad. The purpose is to measure a second coordinate (z in the barrel and r on the disks). The geometry arrangement of the tracker provides at least 9 hits in the strip detector with $|\eta| < 2.4$. Among these hits, at least 4 are two-dimensional measurements with a resolution of 230 and 530 $\mu$m in the TIB and TOB, respectively.

Figure 2.6 shows the expected resolutions of transverse momentum and reconstruction efficiency as a function of pseudorapidity for single muons with transverse momenta of 1, 10 and 100 GeV. The transverse resolution is less than 2% in the barrel and increases in the endcap. The reconstruction efficiency can be as good as 99% for muon in much of the acceptance range.

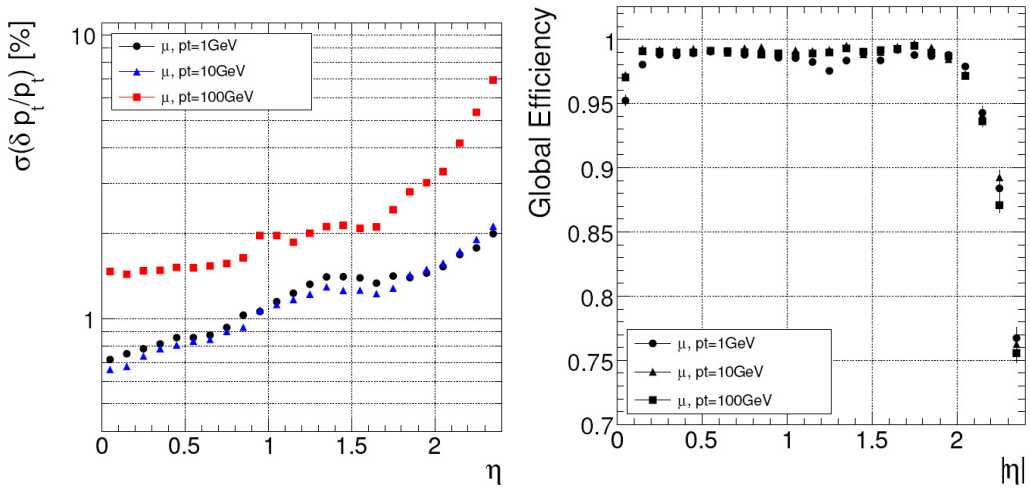


**Figure 2.6:** The tracker transverse momentum resolution and the muon reconstruction efficiency.

### 2.2.3 The Electromagnetic Calorimeter

The CMS electromagnetic calorimeter (ECAL) is a homogeneous scintillator calorimeter. It is built from 61200 crystals in the barrel and 7324 crystals in each of the two endcaps [37]. Crystals are made of fast and radiation-hard lead-tungstate ($PbWO_4$). In order to improve the position resolution of electrons and photons, a preshower detector is placed in front of the endcap crystals. Scintillator light is produced by $PbWO_4$ crystals and converted to electric pulses by avalanche photodiodes (APDs) in the barrel and vacuum phototriodes (VPTs) in the endcaps. The homogeneous ECAL calorimeters provides high granularity and excellent energy resolution, which makes detection of two photons from the postulated Higgs boson decay possible.

#### ECAL layout and mechanic

As shown in Figure 2.7, the CMS ECAL comprises 3 parts: the ECAL barrel (EB) covering $|\eta| < 1.479$, the ECAL endcaps (EE) extending from $1.497 < |\eta| < 3.0$ and the preshower detector placed in front of the ECAL endcaps. The EB is segmented by 360 folds in $\phi$ and $2 \times 85$ folds in $\eta$. The crystal front face centers are at a radius of 1.29 m. In order to avoid cracks aligned with particle trajectories, the crystal axes make a small angle ($3^0$) with respect to the vector from a nominal interaction vertex, in both $\phi$ and $\eta$ projections. In the EB, the crystals of each half-barrel are grouped in 18 supermodules (spanning $20^0$ in $\phi$). Each supermodule comprises four modules. The first module has 500 crystals and each of the 3 remaining modules contains 400 crystals. Inside a module, crystals are grouped in submodules of $2\times5$ crystals to simplify the construction and assembly. The EE detector is identical in both sides. Each side is divided into 2 halves in a "D" ("Dee") shape. Each Dee has 3662 crystals organized in groups of $5\times5$ crystals called the supercrystal. Therefore,

each Dee consists of 138 standard supercrystals and 18 special partial superclusters on the inner and outer circumferences.

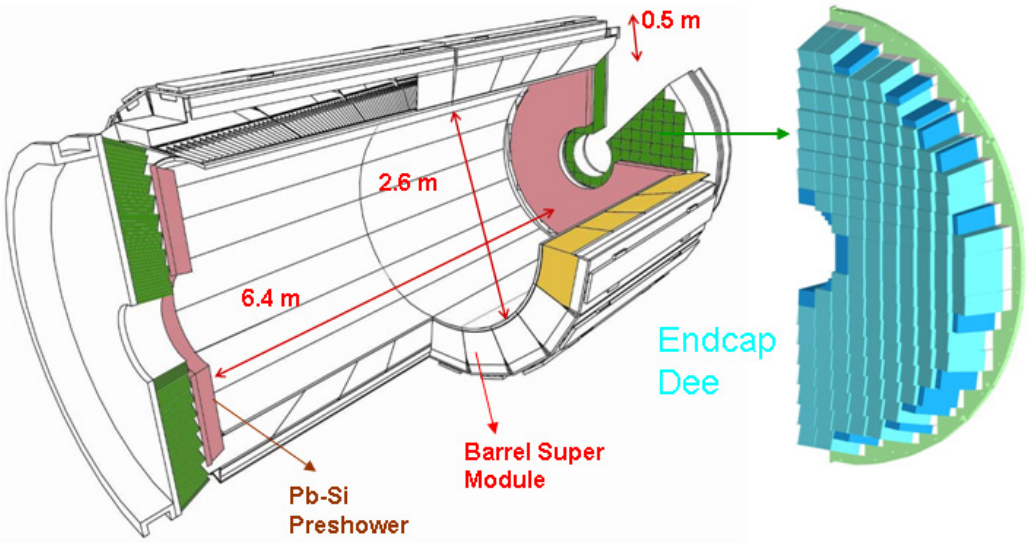


**Figure 2.7:** The ECAL layout.

### Lead-tungstate crystals

The $PbWO_4$ crystal is an appropriate choice for building a fine granularity and a compact calorimeter. It has a high density (8.28 $g/cm^3$), a short radiation length (0.89 cm) and a small Molière radius (2.2 cm). Its scintillation time is short. About 80% of the scintillation light is emitted in 25 ns, which is the LHC bunch crossing interval. However, the light output is relatively low and varies with temperature change (-2.1%$^0C^{-1}$ at $18^0$C). The scintillation emission spectrum has a broad maximum at ~420-430 $\mu$m, which matches the wavelength range of good quantum efficiency of APDs and VPTs. In the barrel, the crystal front face cross-section is 22×22 mm$^2$ or approximately 0.0174×0.0174 in $\eta - \phi$ space. This size is about the Molière radius. The crystal length is 230 mm corresponding to 25.8 $X_0$. Most of the crystal faces are polished except one lateral face in order to make the light collection uniform. In the endcap, the crystals have a rear face cross section of 30×30 mm$^2$, a front face cross

649 section of 28.62×28.62 mm$^2$ and a length of 220 mm (24.7 $X_0$). Figure 2.8 shows a
650 barrel and a endcap crystal and attached photodetectors.

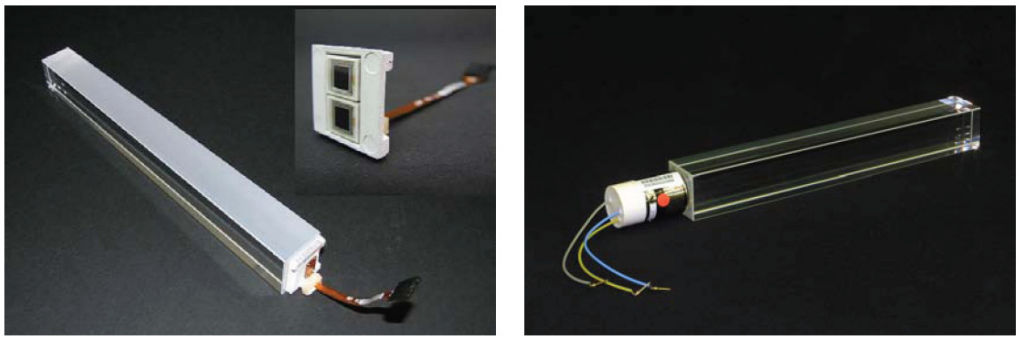

**Figure 2.8:** ECAL crystals and photodetectors.

651 ### The ECAL Photodetectors

652 The photodetectors are attached to the end of scintillator crystals and convert scin-
653 tillation light to electronic pulses. The requirements for a photodetector are fast,
654 radiation tolerant and able to operate in the longitudinal 4 T field. The choices of
655 photodetector technologies, APD for the barrel and VPT for the endcap, are driven
656 by the configuration of the magnetic field and the expected level of radiation. VPTs
657 have lower quantum efficiency and internal gain compared to the APDs. However,
658 this drawback is compensated by their larger surface coverage on the back face of the
659 crystals. A pair of APDs is attached to a crystal and each APD has an active area of
660 5×5 mm$^2$. Each VPT has a diameter of 25 mm and an active area of approximately
661 280 mm$^2$. One VPT is glued to the back of each crystal.

662 ### Preshower Detector

663 The main purpose of the preshower is to provide $\pi_0 - \gamma$ separation. At high rapidity,
664 two photons from $\pi_0$ decays are close together and not resolved in ECAL crystals.

Therefore, $\pi_0 s$ are recognized as fake photons and contribute to the backgrounds in a analysis with photon. A high granularity silicon preshower detector resolves these two photons; thus the backgrounds from $\pi_0$ are reduced. In the Higgs search in diphotons channel, since about half of the Higgs decays results in one photon in the ECAL endcap, the fake photon reduction in the ECAL endcap is necessary to suppress the overall background.

The preshower detector is a sampling calorimeter, which is located in front of the endcap ECAL and covers a fiducial region $1.653 < |\eta| < 2.6$. It consists of two lead layers to initiate electromagnetic showers from incoming photons or electrons. A silicon-strip plane with a pitch of 2 mm is placed right after each lead radiator to measure the deposited energy and the transverse shower profiles. The orientations of the strips in the two planes are orthogonal. Figure 2.9 shows the layout of preshower sections. Total material thicknesses before the first and the second silicon sensor plane are 2 $X_0$ and 1 $X_0$, respectively. Therefore, about 95% single incident photons start showering before reaching the second sensor plane. The energy deposited in 2 mm pitch silicon strips is used to determine the impact position of electromagnetic showers using a charge-weighted-average algorithm. The accuracy is very good, $\sim$300 $\mu$m at 50 GeV. This energy measurement is also used in the correction of energy measured by crystals, which preserves the excellent energy resolution of the ECAL.

**Energy resolution**

The ECAL energy resolution is parametrized as:

$$(\frac{\sigma}{E})^2 = (\frac{S}{\sqrt{E}})^2 + (\frac{N}{E})^2 + C^2 \tag{2.2}$$

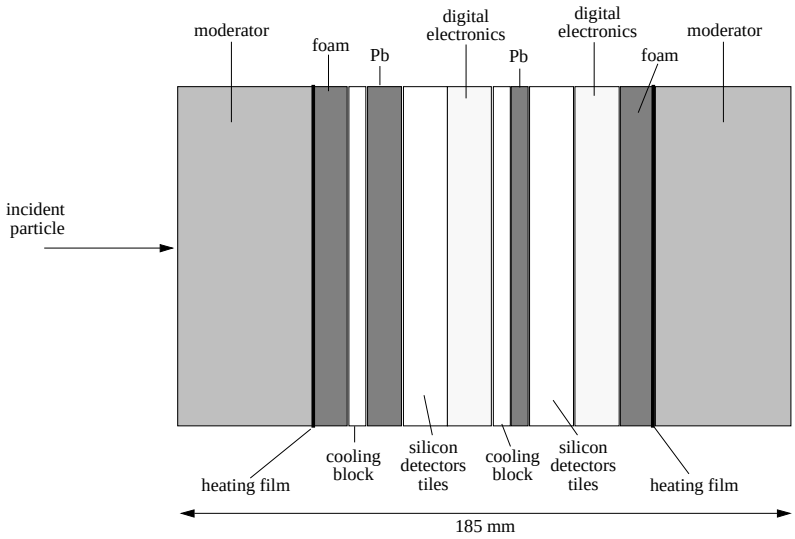


**Figure 2.9:** Arrangement of the preshower layers.

where S is the stochastic term, N is the noise term, and C is the constant term. This parametrization is valid if the shower leakage from the rear of the calorimeter is less important (energy is below about 500 GeV). The contribution to S comes from fluctuations in the lateral shower containment, photostatistics and energy deposit in the preshower absorber (if present). The electronic, digitization and pileup noises contribute to the noise term. The constant term is caused by non-uniformity of the longitudinal light collection, intercalibration errors and leakage of energy from the back of the crystal.

The ECAL energy resolution is measured in the 2004 test beam for electron beam with momentum between 20 and 250 GeV/c. The result is showed in Figure 2.10, in which the stochastic, noise, constant terms are 2.8%, 0.12% and 0.3%, respectively. For an unconverted photon with shower energy $\sim$ 100 GeV, the constant term dominates. Therefore, the ECAL energy resolution depends strongly on the quality of the calibration. The particle energy in the ECAL is estimated by [38]:

$$E = F \times \sum_{cluster crystal} G(GeV/ADC) \times C_i \times A_i, \tag{2.3}$$

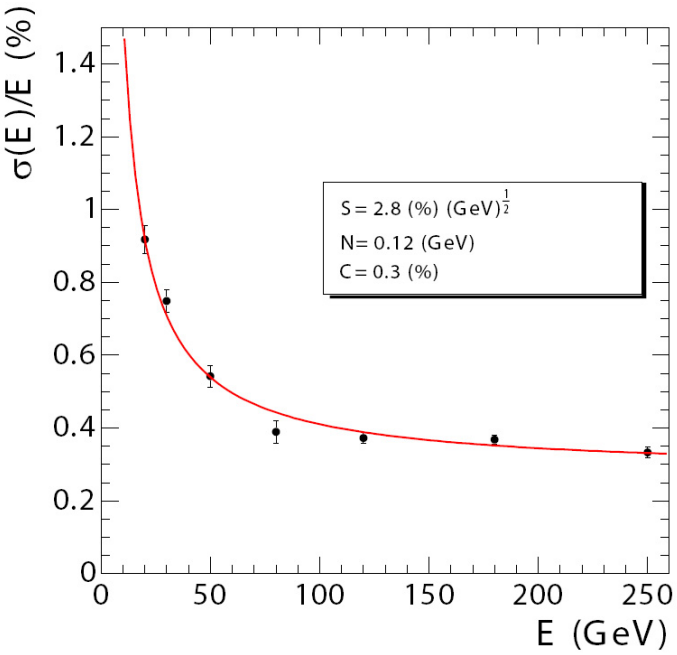


**Figure 2.10:** ECAL energy resolution.

where F is the additional energy correction factor, which depends on particle type, energy and pseudorapidity. For electron, this factor takes into account for the shower leakage and the bremsstrahlung losses; G is the ECAL energy scale for ADC to GeV conversion; $A_i$ are the reconstructed amplitudes in ADC counts; and $C_i$ are the inter-calibration constants, which come from channel-to-channel variation. Details at the method to estimate $C_i$ and G using the collision data are discussed in [38].

### 2.2.4 The Hadronic Calorimeter

The CMS hadronic calorimeter (HCAL) is a sampling calorimeter made of layers of dense absorber material and active material. The absorber material is brass or steel and the active material is scintillator. The hadronic calorimeter is vital for jets and missing transverse energy measurements. It includes four subsystems: the Hadronic Barrel (HB), the Hadronic Endcap (HE), the Hadronic Outer (HO) and

the Hadronic Forward (HF) calorimeters.

The HB covers region $|\eta| < 1.3$ and is placed in the gap between the ECAL outer extent (R = 1.77 m) and the magnet coil inner extent (R = 2.95 m). Its thickness is limited to 5.8 hadronic interaction lengths at $\eta = 0$ and increases to 10 interaction lengths at $|\eta| = 1.2$ [37]. Therefore, the HO, which is placed outside the solenoid and covers $|\eta|$ <1.26, is used to catch the energy leakage from HB. The HE covers region $1.3 < |\eta| < 3.0$ and the HF, placed outside the magnet at z = 11.2± (from the interaction point to their front faces), covers the forward region $3 < |\eta| < 5.2$.

The HF calorimeter uses Cherenkov-based, radiation-hard technology consisting of quartz fibers and steel. The fibers are parallel to the beam direction. Half of the fibers are long fibers extending the full length of the HF detector (165 cm), while other half of the fibers are shorter which stop at a distance of 22 cm from the front face of the HF. The purpose of this arrangement is to distinguish the electromagnetic and hadronic showers, since a electromagnetic shower starts to develop earlier than the hadronic shower and deposits most of its energy in the long fibers while a hadronic shower starts late and deposits most of its energy in the short fiber.

The HB and HO are segmented in towers of 0.087×0.087 in $\eta - \phi$ space. The HE has the same granularity up to $|\eta| = 1.74$, after that the $\eta$ segmentation varies from 0.09 to 0.35 and the $\phi$ segmentation is 0.175. In the HF, the segmentation is 0.175×0.175 and 0.175×0.35 at $|\eta| < 4.7$ and $|\eta| > 4.7$, respectively [9]. Figure 2.11 shows the segmentation of the HCAL.

Light from the scintillation tiles is carried out by the embedded wavelength-shifting fibers. There are 17 scintillation layers in each HB and HE tower. The light of all scintillation layers are optically added in the HB. In the HE, the towers

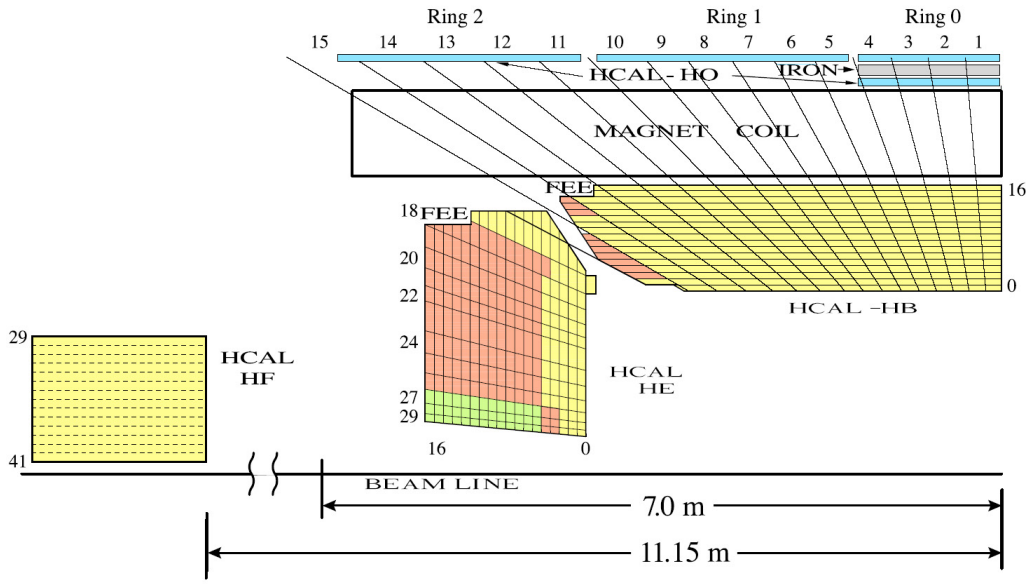


**Figure 2.11:** The schematic view of the CMS hadronic detector [9].

are divided in depths and the light from scintillation layers at the same depth are added. Finally, light signals are read by hybrid photodetectors (HPD). In the HF, lights from the fibers are collected by photomultipliers (PMT) housed in the read-out boxes.

### 2.2.5 The Muon Detector

The CMS muon detectors are gaseous detectors used for muon trigger, identification, charge and momentum measurements. They are composed of 1400 chambers of 3 types: 250 drift tube chambers (DT) in the barrel ($|\eta|$ <1.2), 468 cathode strip chambers (CSC) in the endcap disks (1.2< $|\eta|$ <2.4) and 610 resistive plate chambers (RPC). The RPCs are mounted together with both the DT and CSC. The DT technology is the choice for the barrel because of small neutron-induced background, low muon rate and uniform magnetic field (mostly contained in the return yoke) in this region. In the endcap, the muon rates and background levels are high and the

750 magnetic field is large and non-uniform. Thus, cathode strip chambers (CSC) are
751 used.

752 The DT chambers are installed in hollows of the 5-wheel return yokes and orga-
753 nized in 4 stations. In the first three stations, each DT chamber composes 12 layers
754 of drift tubes arranged in 3 groups of 4. The two of these groups have wires along
755 z used to measure the $\phi$ coordinate and the other group measures the z coordinate.
756 There are no z measuring layers in the outermost DT station.

757 The CSC system is arranged in 4 stations perpendicular to the beam pipe and
758 mounted on the endcap disks. Each CSC chamber is built from 6 cathode planes
759 and anode wires. In order to measure the position of a muon hit, cathode planes are
760 segmented into narrow trapezoidal strips projecting radially from the beam line and
761 anode wires are aligned perpendicularly to the strips.

762 The RPCs are fast gaseous detectors, which are added to both barrel and endcap
763 (up to $|\eta|$ <1.6). Their purposes are to provide fast, independent, and highly-
764 segmented trigger and help to resolve ambiguities when there are multiple hits in
765 a chamber. In the barrel, 6 layers of RPCs are embedded, 2 in each of the first
766 2 stations, and 1 in each of the last 2 stations. In the endcap region, there is a
767 plane of RPCs in each of the first 3 stations. This arrangement allows the trigger to
768 use the coincidences between stations for reducing backgrounds, improving the time
769 resolution of bunch crossing identification, and for achieving a good $p_T$ resolution.

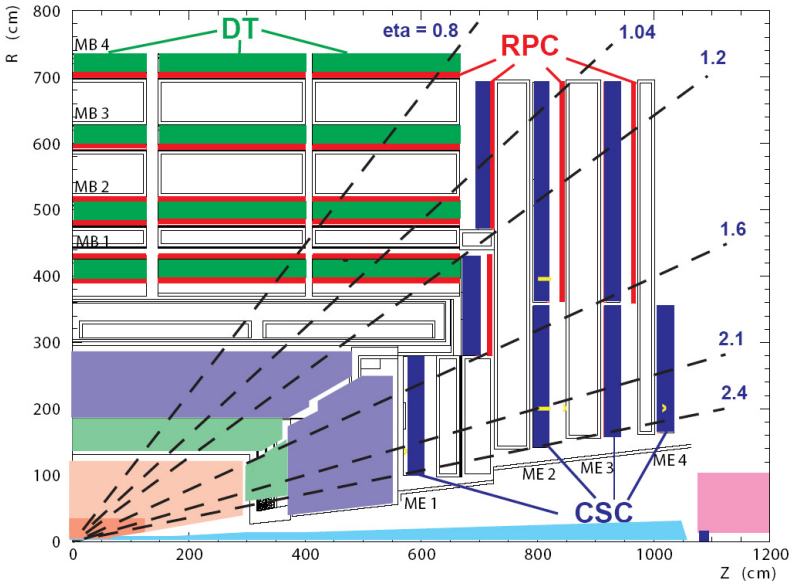


**Figure 2.12:** The muon detector layout [10].

### 2.2.6 The CMS trigger

At the design luminosity, $10^{34}$ cm$^{-2}s^{-1}$, the LHC crossing rate is 40 MHz with about 20 pp simultaneous collisions in each crossing. Because of this enormous rate, it is impossible to store all the events, and a trigger system is used to reduce dramatically the rate (by a factor $10^6$) by selecting just most interesting events for physics analysis. The CMS trigger is a 2-level architecture trigger. The Level-1 trigger (L1) is built from fast custom hardware processors with the maximum bandwidth of 100 kHz (the practical maximum output rate is 30 kHz, assuming an approximate safety factor of three). The L1 trigger system is divided in 3 subsystems: the L1 calorimeter trigger, the L1 muon trigger, and the L1 global trigger. The muon trigger system comprises 3 subsystems corresponding to 3 muon subdetectors, the Drift Tube Trigger in the barrel, the Cathode Strip Chamber (CSC) trigger in the endcap and the Resistive Plate Chamber (RPC) covering both barrel and endcap.

Trigger information from the DT, CSC and RPC trigger systems is combined at

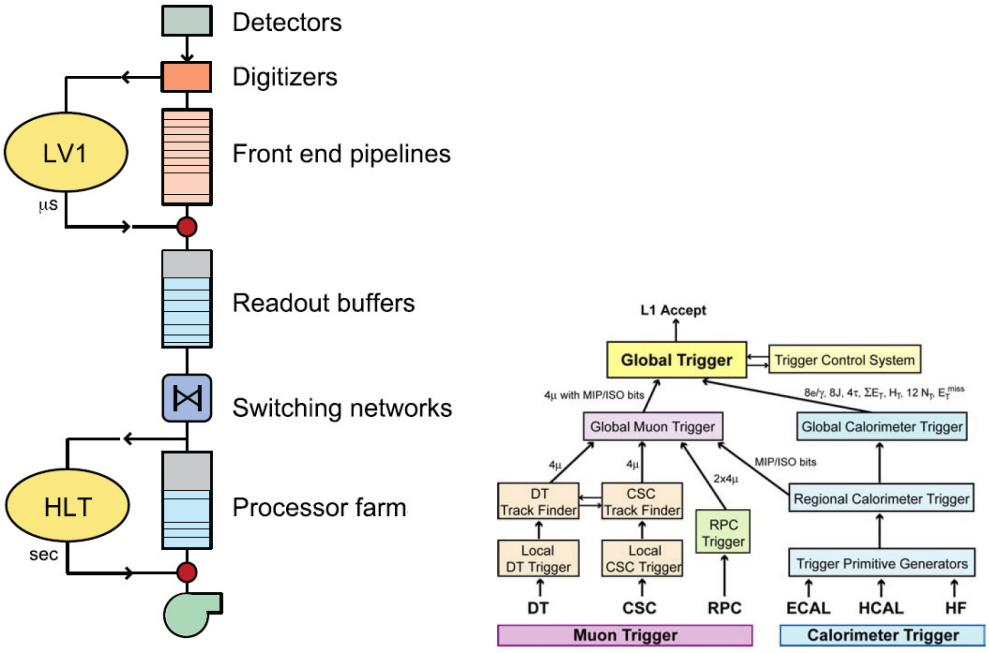


**Figure 2.13:** The structure of the CMS trigger (left) and the L1 trigger (right) [10].

the L1 global muon trigger and sent to the L1 global trigger. Up to 4 candidates from each of the DT and CSC triggers and up to 8 candidates (4 in the barrel, and 4 in the endcap) from the RPC trigger are sent to the L1 global muon trigger which in turn sends 4 highest quality muons to the L1 global trigger. In the calorimeter trigger, the trigger primitives constructed from the energy sums in the trigger towers of the ECAL, HCAL and HF are generated by the Trigger Primitive Generator (TPG). The TPG information is transmitted to the Regional Calorimeter Trigger (RCT), which combine them together into regions of the size of 4 x 4 towers in the central region and somewhat larger size in the forward direction. These regions are transferred to the Global Calorimeter Trigger (GCT). The GCT finds isolated or non-isolated electron/photon, tau, jet candidates and the sum of transverse energy, performs the candidate sorting based on their ranks and forwards the top 4 of each type to the global trigger. The total transverse energy and total missing energy vector are also calculate by the GCT. Finally, the GCT information is forwarded to the global trigger, which issues the trigger decision. This trigger decision is transmitted to all of

the subdetector front-end and readout systems by the Trigger Timing and Control system. The L1 pipeline data storage time is 3.2 $\mu$s. Therefore, the L1 trigger calculations is limited in many cases in less than 1 $\mu$s [39].

The High-Level Trigger (HLT) is a software system implemented in a filter farm of commercial processors (Event Filter Farm) which reduces further the event rate from L1 trigger to the order of 100 Hz before data storage. The HLT access to complete read-out data via a 100 Gb/s switching network. Thus, it has the capacity to perform sophisticated calculations based on reconstruction algorithms similar to those of the off-line analysis.

# Chapter 3

# Event Reconstruction

The purpose of this chapter is to overview the reconstruction of objects from signals in sub detectors. These signals are produced when particles from the interaction points transverse through detector materials. Trajectories of charge particles are measured in the tracker (Section 3.1). Measurements of muon tracks use information from both the tracker and the muon chambers (Section 3.3). Electrons and photon are measured in the electromagnetic calorimeter (ECAL) (Section 3.5). The electron track are reconstructed in the tracker. Finally, jets and missing transverse energy are reconstructed from the energy deposits in the calorimeter towers (Section 3.4). A calorimeter tower is a combination of a hadronic (HCAL) tower and electromagnetic crystals located in front of this HCAL tower.

## 3.1 Track Reconstruction

Tracks are reconstructed by Combinatorial Track Finder (CFT) following these steps: local reconstruction, seed generation, pattern recognition, final track fit and track selection. The track reconstruction in CMS begins with hits reconstructed by local reconstruction in the pixel and strip detector. The seed generation step defines initial trajectory parameters and their uncertainties. At least 3 hits or 2 hits and a beam constraint are required to identify five parameters needed for trajectory building. Reconstructing track seeds from the most inner layer of the tracker is more preferred due to higher density of the read-out channel per square unit and less interaction between particle and material. These conditions ensure precision of the initial track parameter estimation. These are common seeding types used in CMS: pixel triplets, pixel and strip pairs with vertex constraint or with beam-spot constraint, strip-only pairs with beam-spot constraint [40].

The pattern recognition is based on the Kalman filter [41]. Beginning with a coarse estimation of track parameters from the track seeding, the filter proceeds from layer to layer to find compatible hits. If a hit is found, it is included in the trajectory and the track parameters are updated with information from this hit. The iteration stops when the outermost layer is reached or no compatible hit is found. This step results in number of track candidates satisfying requirements on normalized $\chi^2$ and number of valid and invalid hits. The final track fit refits the track candidates for a full track information.

The track selection step reduces large number of fake tracks. In the current CMS implementation, the CFT iterates for 6 times [42]. After an iteration, the unambiguous track clusters assigned to tracks are removed from the cluster iteration

used in the next iteration. The tracks which is likely fake are also rejected. The remaining tracks are assigned a quality flag based on restriction on normalize $\chi^2$, the longitudinal and transverse impact parameters with respect to the beam-spot, and their significance. Poorly quality tracks are further rejected and highPurity flag is assigned for tracks that pass the tightest selection [42]. Figure 3.1 shows the impact parameter resolution in 2010 pp collision data.

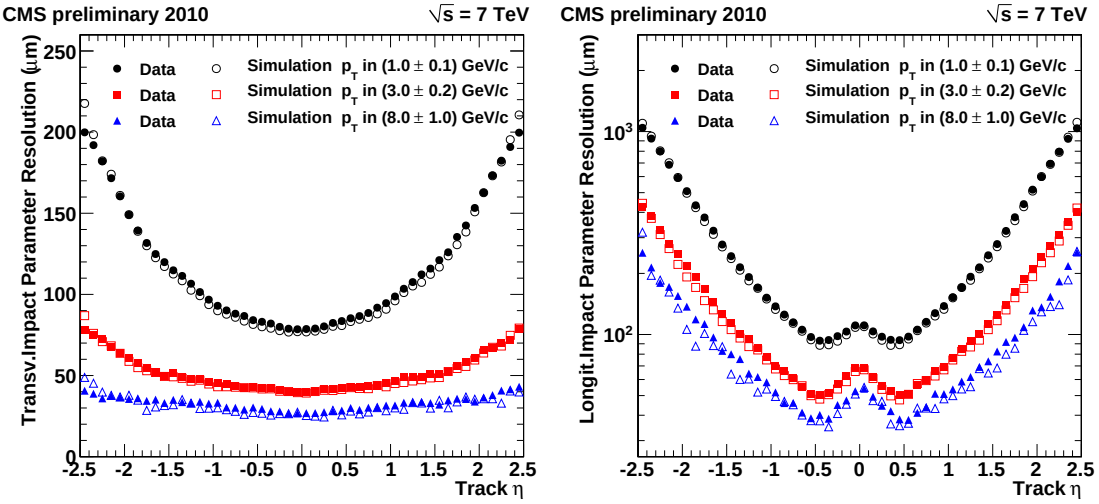


**Figure 3.1:** The track impact parameter resolutions [11]

## 3.2 Vertex Reconstruction

The primary vertex reconstruction finds the location of interaction vertex and its uncertainty. The main idea is to use reconstructed tracks which are close together when comparing their impact parameters. The tracks are required to originate from the primary interaction region and satisfy criteria on the transverse impact parameter significance with respect to the beam line, number of strip and pixel hits, and the normalized $\chi^2$. The next step is to form vertex candidates by grouping tracks that are separated in $z_0$, z coordinate of the impact point, by less than $z_0$ <1 cm compared

to their closet neighbor.

A vertex fitting is performed by an adaptive vertex fit [43] on vertex candidates containing at least two tracks. The best estimations of vertex parameters (position and covariance matrix) are found together with parameters to indicate fit quality, for example $\chi^2/n_{dof}$ and the track weights. Track weights are from 0 to 1 based on the track compatibility with the common vertex. The reconstruction efficiency is approximate 100% for primary vertex containing more than 2 tracks with transverse momenta greater than 0.5 GeV. In the minimum bias data at 7 TeV, the x(y) and z resolution are close to 25 $\mu$m and 20 $\mu$m for primary vertex with more than 30 tracks [11].

## 3.3 Muon reconstruction

Muon track reconstruction combine hits in the tracker and in the muon chambers. Muon tracks are reconstructed separately in the silicon tracker and muon chambers (stand-alone muon track). These are merged by outside-in (global muon reconstruction) or inside-out (tracker muon reconstruction) algorithms. In the global muon reconstruction, a standalone muon track is matched with a tracker track and the hits of those tracks are combined in a common fit to find the global muon track. This method improves the momentum resolutions of high $p_T$ tracks ($p_T \geq$200 GeV) compared to tracker-only fit. In the tracker muon approach, tracker tracks with $p_T$ >0.5 GeV/c and p>2.5 GeV/c are considered as muon candidates and they are extrapolated to the muon systems to find a match muon segment found from DT or CSC hits. Energy loss and uncertainty due to multiple scattering are considered in the extrapolation. If the matching is found, the tracker track is considered as

tracker-muon track. Because the method requires only a matched single muon segment in muon chambers, it has higher reconstruction efficiency for low $p_T$ tracks compared to the global muon reconstruction.

About 1% of muon from collisions fail to be reconstructed by two methods above but are found by the stand-alone tracker only approach [12]. Finally, muon candidates found by all three algorithms are merged to a single collection. Each candidate contains available information from the stand-alone, the tracker-track and the global fit. If two candidates are found by Tracker Muon and Global Muon and share the same tracker track, they are merged into a single candidate. If a standalone-muon track shares a muon segment with a tracker muon and is not included in a global muon track, it is merged to the tracker muon. Figure 3.2 shows the reconstruction efficiency of the global muon.

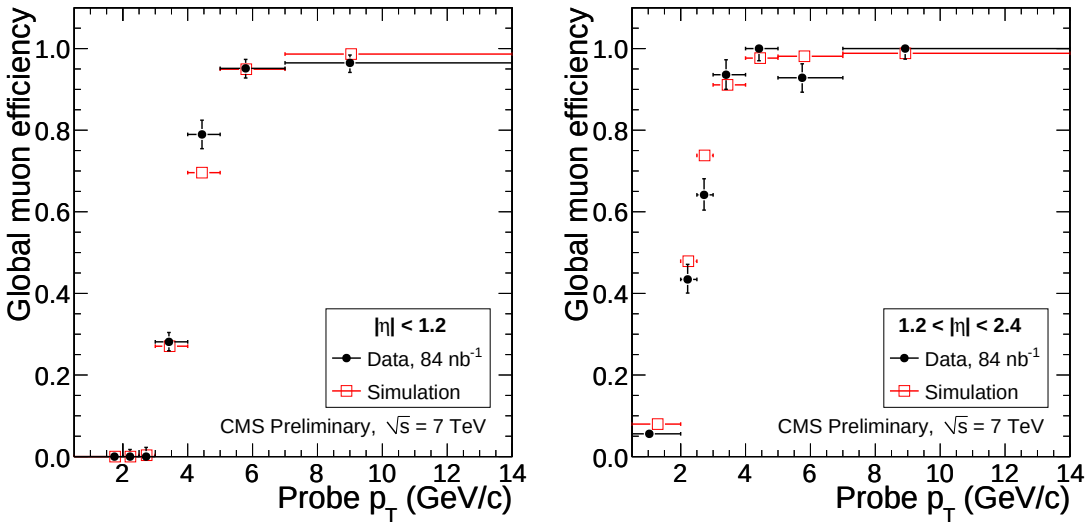


**Figure 3.2:** Muon reconstruction efficiency [12]

## 3.4 Jet and Missing ET reconstruction

The fragmentation of quarks and gluons in the final state results in a stream of collimated particles. A calorimeter clustering algorithm clusters energy deposit in the calorimeter tower to form a jet. A calorimeter tower is a combination of HCAL cells and geometrically corresponding ECAL crystals. One HCAL cell corresponds to 5×5 ECAL crystals in the barrel ($|eta|$ <1.4). In the endcap, the HCAL-ECAL mapping is more complex. A successful algorithm should be collinear-safe and infared-safe [44]. Collinear-safe requires that the outcome remains unchanged if the energy of a original single particle is distributed among two collinear particles. Infrared-safe means that the result of the jet finding is stable against addition of soft particles. Below are some of the algorithms used in CMS:

- Iterative cone: this is a simple cone-based algorithm which performs iterative searches for stable cones. Starting from a seed crystal or particle, all inputs within $\sqrt{\delta\eta^2 + \delta\phi^2}$ ≤R are associated with a jet. R is the cone-size parameter (popular choice is 0.5). If the cone geometric center agrees with the ($\eta$, $\phi$) location of the sum of the constituent four vectors, a jet is found. This algorithm is not collinear-safe and infared-safe but it is fast and has predictable calculation time. Thus, it is implemented in the HLT.

- Midpoint cone [45]: this method uses iterative cone technique to find stable cones. However, there are two improvements to address the infared-safe condition. Midpoints between each pair of (proto-)jets, which are closer than twice the cone radius R, are uses as additional seeds and each input can initially be associated with several protojets. A splitting and merging algorithm is implemented to ensure that each input appears in one jet only. Despite these improvements, the algorithm is not infared-safe for pQCD order beyond

NLO [45].

- $k_T$ algorithm: the clustering is decided by distance quantities assigned for each protojet

$$d_i = (E_{T,i}^2)R^2 \tag{3.1}$$

$$d_{ij} = min(E_{T,i}^2, E_{T,j}^2 R_{ij}^2) \tag{3.2}$$

$$R_{ij}^2 = (\eta_i - \eta_j)^2 + (\phi_i - \phi_j)^2 \tag{3.3}$$

where $E_{T,i}$ is the transverse energy of $i^{th}$ protojet, $R_{i,j}^2$ is the distance between two protojets. $R^2$ is a dimensionless parameter. The next step is to sort the list of $d_i$ and $d_{ij}$ and finds the smallest values. If the smallest value is $d_i$ type, the corresponding protojet is considered as a jet and removed from the list. If the smallest value is $d_{ij}$, the protojet pair is recombined. The distances are recalculated and the whole procedure is repeated. The search stops when the list is empty. There is an extension to this method called anti-k$_T$ algorithm which uses these distance definitions [46].

$$d_{iB} = E_{T,i}^{2p} \tag{3.4}$$

$$d_{ij} = min(E_{T,i}^{2p}, k_{T,j}^{2p})\frac{R_{ij}^2}{R^2} \tag{3.5}$$

p is a parameter to tune the relative power of the energy and geometrical scales, $R_{ij}$. For p=1, this returns to the normal $k_T$ algorithm and for p>0, the performance is similar to the $k_T$ method. The anti-$k_T$ jet-clustering algorithm corresponds to p=-1.

- SISCone (Seedless Infrared-Safe Cone) is a jet algorithm which is collinear- and infrared-safe to all orders of pQCD. The calculation time is slightly higher compared to the Midpoint Cone algorithm [44].

There are four types of jets reconstructed in CMS. The differences between these are the combination of subdetector information to provide inputs for the jet clustering algorithm. The calorimeter jets are reconstructed from energy deposit in calorimeter towers by the clustering methods describe above. Utilizing the excellent momentum reconstruction of the tracker, calorimeter jets are combined with nearby charged tracks reconstructed in the tracker to form jet-plus-track jets [47]. The $p_T$ respond and the energy resolution of jets are improved due to better momentum measurements in the tracker. The particle flow algorithm is used to reconstruct PFlow jets [48]. A list of all particles reconstructed by all subdetectors is found and PFlow jets are reconstructed from this list. Finally, track jets are reconstructed based on well measured tracks in the central tracker [49].

Jet energy measured in the detector is corrected for a better measurement of particle jet energy. CMS adopts factorized multi-step procedure for the jet energy correction: offset, relative and absolute corrections [50]. The offset correction removes the unwanted energy due to electronic noise and pile-up. The relative correction uniforms the jet respond vs jet $\eta$ with respect to a central control region chosen as a reference. Finally, the variation of jet respond vs. $p_T$ is removed by the absolute correction:

$$E_{corr} = (E_{uncorr} - E_{offset}) \times C_{Rel}(\eta, p_T^{''}) \times C_{Abs}(p_T^{'}) \tag{3.6}$$

where $p_T^{''}$ is the jet transverse momentum given by offset correction and $p_T^{'} = p_T^{''} \times C_{Rel}(\eta, p_T^{''})$ is the transverse momentum given by the offset and relative correction. At the initial stage of LHC running, the correction is done in MC simulation. It can also be done using physics processes from the pp collision (dijet and photon+jet balance). Figure 3.3 shows the total jet energy scale uncertainty in 2010 collision data at 7 TeV. Current CMS analyses use conservative 10% jet energy scale uncertainty for calorimeter jet and 5% uncertainty for jet-plus-track and PFlow jets with additional

2% per unit of rapidity.

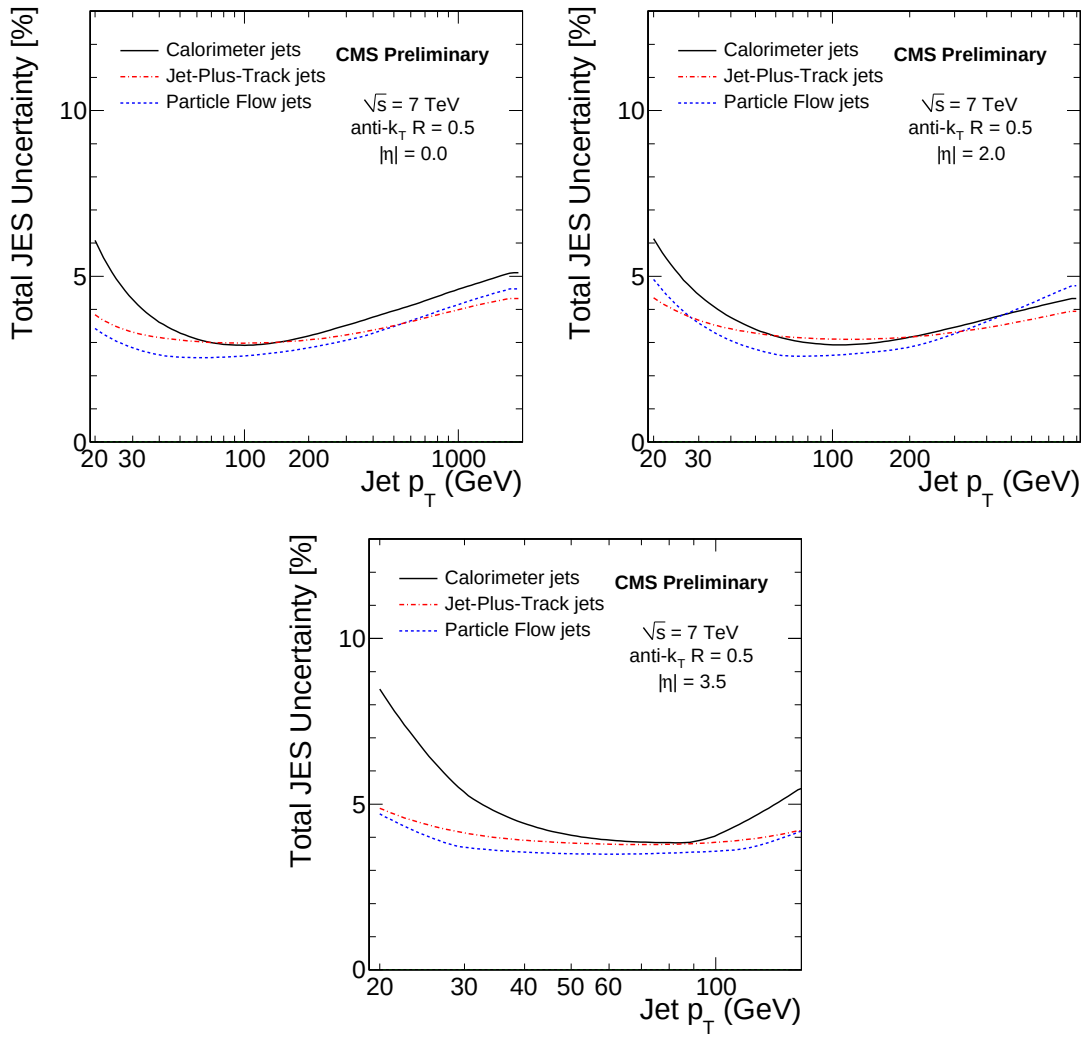


**Figure 3.3:** Jet energy scale uncertainty [13]

961

962 Weakly interaction particles, for example, neutrinos, transverse the detector with-
963 out depositing their energy. The missing transverse energy is an indication of the
964 production of such particles in the pp collision. The missing transverse energy is
965 defined as [51]:

$$\not\!\!E_T = -\sum n(E_n \sin\theta_n \cos\phi_n \vec{i} + E_n \sin\theta_n \sin\phi_n \vec{j}) = \not\!\!E_x \vec{i} + \not\!\!E_y \vec{j} \qquad (3.7)$$

where n runs over all calorimeter input object, for example, energy deposit in towers or generated-level particle energy, $\vec{i}$, $\vec{j}$ are the unit vectors in the direction of the x and y axes. If there is no missing transverse energy from physics processes, the $\not\!\!E_x$ and $\not\!\!E_y$ distribute as Gaussians with zero mean and standard deviation $\sigma$, while the magnitude of missing transverse energy vector, $\not\!\!E_T$, distribution has the shape described by $\frac{2\pi}{\sigma}\theta(\not\!\!E_T) \times G(\not\!\!E_T, 0, \sigma)$. In this formula, $\theta(\not\!\!E_T)$ is the step function and G is the Gaussian function. The missing transverse energy resolution is estimated by the quadrature sum of the noise term A, stochastic term B and constant term C [51]:

$$\sigma(\not\!\!E_T) = A \bigoplus B\sqrt{\sum E_T - D} \bigoplus C(\sum E_T - D), \tag{3.8}$$

where $\sum E_T = \sum nE_n \sin\theta_n$ is the Scalar Transverse Energy and D is the offset caused by the noise effect and pile-up on $\sum E_T$.

CMS use three types of $\not\!\!E_T$: calorimeter-tower based (CaloMET), calorimet-jet based (MHT) and particle flow based (PFMET) $\not\!\!E_T$. The CaloMET and MHT are corrected in sequence for muons, jet energy scale effect, taus, underlying event/pile-up. Details are described in [51]. Instead of using jet energy scale correction, a track-base correction, which replaces the calorimeter tower respond for charged particle momentum measured in the tracker, is applied for CaloMET [52]. The PF algorithm reconstructs individual particles with high precisions. Thus, the PFMET is calculated from the charged and neutral particle energy deposit without the need of a correction. Figure 3.4 shows the missing transverse energy of multijet events in 7 TeV collision data.

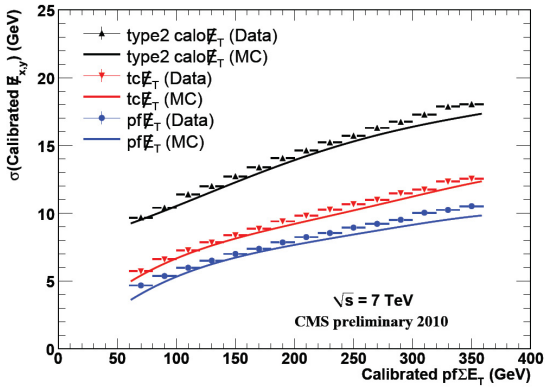


**Figure 3.4:** Jet energy scale uncertainty [14]

## 3.5 Photon and Electron

### 3.5.1 ECAL clustering

The clustering methods used in CMS to reconstruct photon and electron objects are hybrid and island algorithm [53].

- Island algorithm: This algorithm forms clusters of crystals containing deposit energy from a shower around seed crystals. The energy of the seed crystals are above a certain threshold. The clusters are collected one-by-one while the search moves in $\eta$ and $\phi$ directions. Figure 3.5 illustrates the algorithm. Starting from the seed crystal position, it moves in both $\phi$ directions and stops when there is an increase in energy or a hole (very low energy crystal). The search in $\phi$ direction is repeated for each $\eta$ step and in both $\eta$ directions. The algorithm also stops in a $\eta$ direction if it encounters an increase in energy or a hole. In order to cover the energy spread due to radiation, clusters are clustered in a supercluster in a similar way as forming cluster of crystals. Non overlapping clusters around a seed cluster within narrow $\eta$ window and much wider $\phi$ window are collected in a supercluster.

- Hybrid algorithm: The clustering starts from a seed crystal which has maximum energy in the search region and $E_T > E_T^{hybseed}$. Crystals are grouped in 1×3 or 1×5 dominoes aligned in $\eta$ with the seed crystal. If the energy of the central crystal is more than $E_{wing}$, 1×5 dominoes are chosen. The domino grouping proceeds in $N_{step}$ from the seed crystal in both directions (see Figure 3.5). The next step is to cluster these dominoes in $\phi$ requiring that a distinct cluster has a seed domino with $E > E_{seed}$. Finally, a cluster of clusters is found analogous to the super-cluster of island clusters.

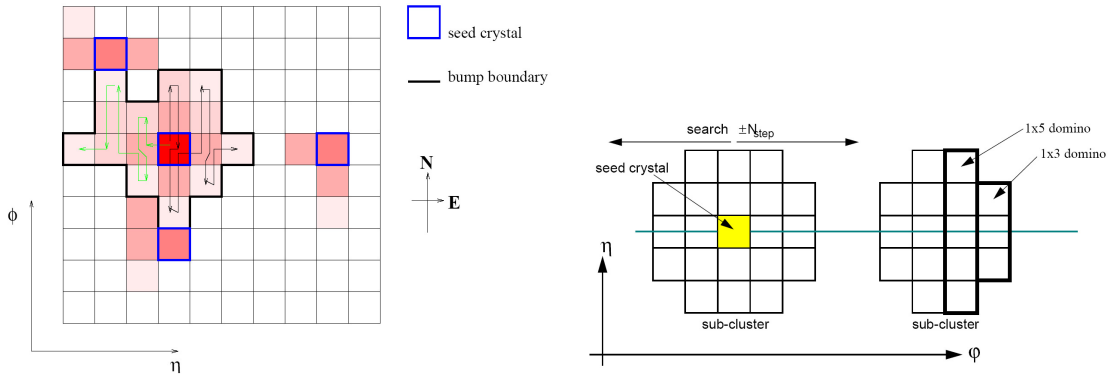


**Figure 3.5:** Island and hybrid clustering algorithm illustration [**?**]

### 3.5.2 Photon candidate

The photon reconstruction starts from summing the photon shower energy deposits in the ECAL crystals. An array of 5×5 (3×3) crystals contains 97% (94%) the incident energy. Summing the energy measured in such fixed arrays gives the best performance for unconverted photons, or for electrons in the test beam [10]. However, the presence of the material in front of the ECAL causes the photon conversions and the energy deposit spread in $\phi$ due to the strong magnetic field (the strong magnetic field bends the electron and positron tracks, and they radiate in tracker material). A cluster of clusters, supercluster, which extends in $\phi$, is built to recover fully the

photon energy. The superclusters are reconstructed by the hybrid algorithm, in the barrel, or the island algorithm, in the endcaps as described above. A small correction ( 1%) is applied to the supercluster energy in other to compensate for the lateral energy leakage due to $3^0$ off-pointing of EB crystal, the interaction with material in front of ECAL.

The R9 variable, defined as the ratio of energy contained in a 3×3 array of crystals (centred at the crystal with the highest deposited energy) to the supercluster energy, indicates the lateral spread of deposit energy. Figure 3.6 shows the R9 variable observed in data at 7 TeV. R9 approaches unity for unconverted photons or photons which convert very close to the ECAL. This quantity determines which method is used for energy calculation. If R9 is above 0.94 (0.95) in the barrel (endcap), the photon energy is the energy of the 5×5 crystal array around the seed crystal (the highest energy crystal). Below this threshold, the energy of the supercluster is the photon energy. In the endcap, the energy deposit in the preshower detector is added to the energy of the ECAL clusters. The superclusters or 5×5 clusters are promoted to be the photon candidates if the HCAL activity around them is low.

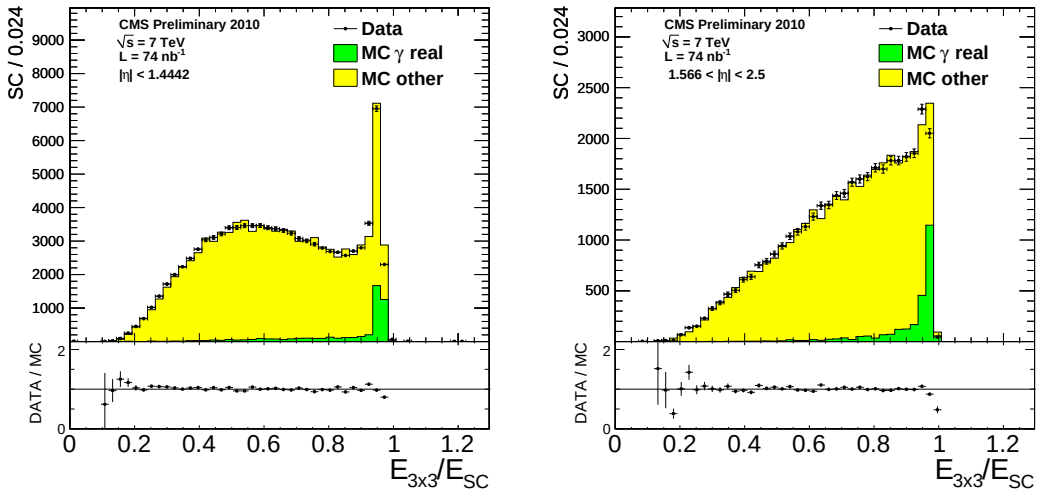


**Figure 3.6:** R9 distribution [15]

### 3.5.3 Photon Identification

As described in the previous section, photon objects are reconstructed from corrected energy deposition of a suppercluster or a 5×5 crystal array. A jet with significant fraction of its energy concentrated in neutral $\pi^0$ or $\eta$ causes energy deposit in ECAL. Therefore, a fake photon is reconstructed. In order to improve the photon purity, a set of identification requirements are applied to photon candidates. These identification requirements are mostly based on the isolation defined as:

- *HadronicOverEM*: The hadronic energy divided by the electromagnetic energy in the supercluster. The hadronic component is computed as the highest energy HCAL `RecHit` within $\Delta R < 0.15$ of the supercluster.
- *Tracking Isolation*: $\Sigma p_T$ of tracks within a hollow cone of $0.04 < \Delta R < 0.40$ about the supercluster.
- *ECAL Isolation*: Sum $E_T$ of ECAL RecHits within a hollow cone of $0.06 < \Delta R < 0.40$ about the supercluster. The "Jurassic" footprint, consisting of a strip of a specified $\eta$ width, is removed from the sum.
- *HCAL Isolation*: Sum $E_T$ of HCAL RecHits within a hollow cone of $0.15 < \Delta R < 0.40$ about the supercluster.

Showers from photons expend in a few crystals from the seed crystal. The weighted width in $\eta$ of the shower is used as an identification variable.

$$\sigma^2_{i\eta i\eta} = \frac{\sum_i^{5\times5} w_i (i\eta_i - i\eta_{seed})^2}{\sum_i^{5\times5} w_i}, w_i = max(0, 0.47 + ln\frac{E_i}{E_{5\times5}}) \tag{3.9}$$

Photons weakly interact with the pixel detector. Therefore, there is no seed in the pixel detector associated with photons. Vetoing on present of a pixel seed is an optional requirement to distinguish between photons and electrons.

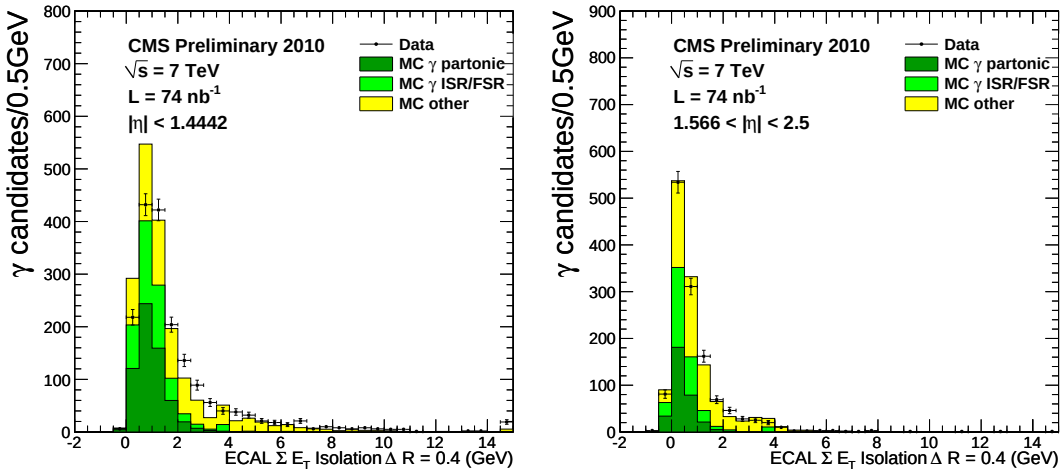


**Figure 3.7:** ECAL isolation [15]

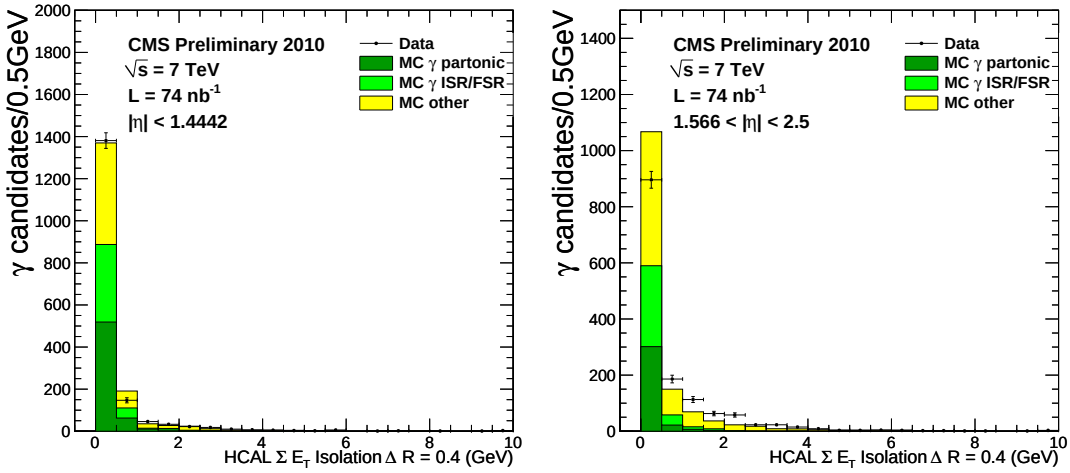


**Figure 3.8:** HCAL isolation [15]

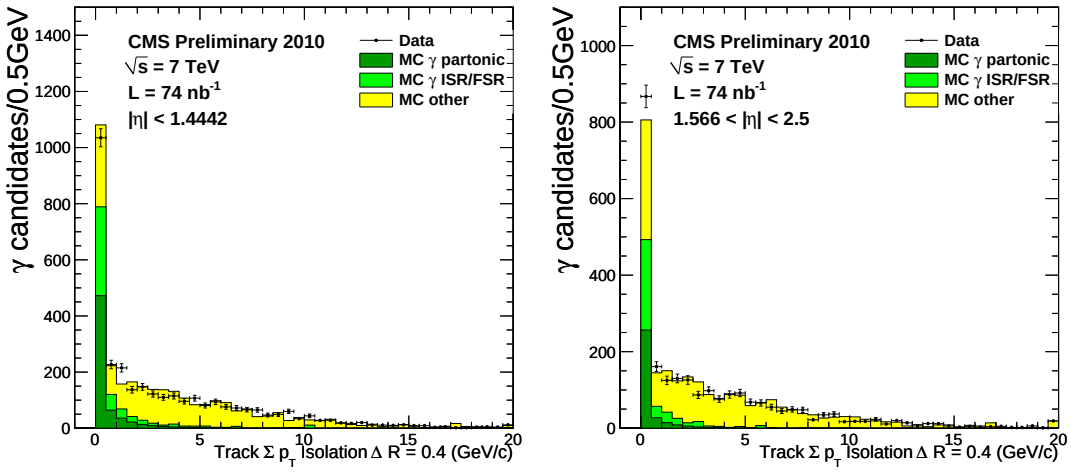


**Figure 3.9:** Track isolation [15]

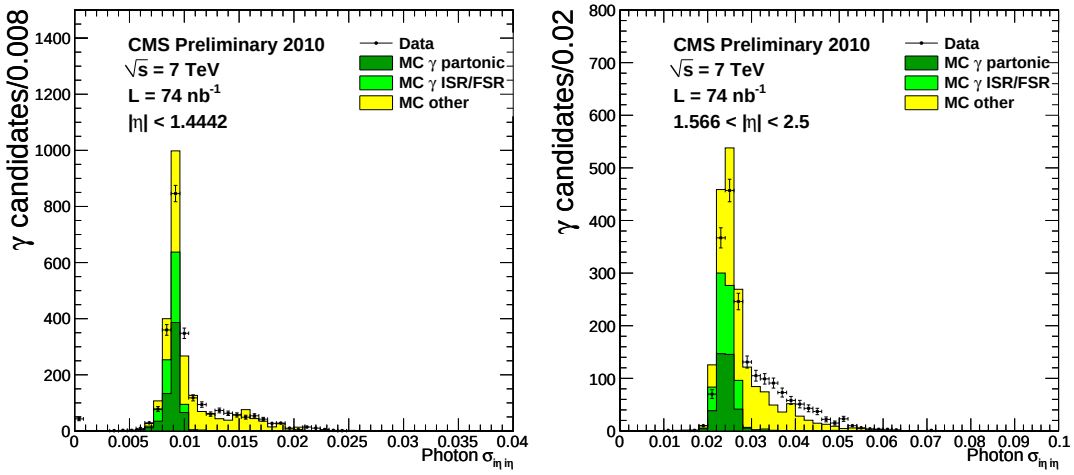


**Figure 3.10:** Shower shape distribution [15]

### 3.5.4 Photon conversion

The amount of material (mostly the tracker) in front of the ECAL is about one radiation length. Thus, a large fraction of photons is converted before reaching the ECAL. Identifying photon conversions benefits the search for H$\rightarrow \gamma\gamma$ in the mass range $110 \leq M_H \leq 150$ GeV/c$^2$. This identification improves the poor ECAL energy resolution due to conversions and helps reduce the leading $\pi^0$ in jets which constitutes

the main irreducible background for the H$\rightarrow \gamma\gamma$ channel [54].

Photon conversions are identified by a pair of an electron and a positron having a conversion vertex (or their closet approach distance is short). The reconstruction of $e^+e^-$ track pairs from conversions combines calorimetric and tracking information. The CMS standard tracking reconstruction are optimized for tracks coming from the primary interaction vertex with pattern recognition starting from seeds found in the pixel detector. This method is not suitable for reconstructing the conversion tracks which originate from conversion points displayed largely from the primary interaction vertex. A new tracking technique is developed [54]. In this approach, at first, a predicted track path is found from the ECAL energy deposits (basic cluster) and the origin of the CMS reference frame. Pairs of hits are sought in the two outermost layers of the tracker in a small window from the hypothesis tracks. The search is extended to the third layer if no hit is found in the two outermost layers. If a compatible hit exists in these layers, the predicted track state is updated, taking this hit as the starting point. The search continues moving inward to the next layer until another hit is found. Using pattern recognition and trajectory building, seed tracks are formed from these pairs of hits. The initial seeds are transformed into a set of trajectory candidates (limited to 5 in order to avoid large combinatorics). The result of the inward tracking step is a list of tracks and only the opposite-charge pair with largest number of reconstructed hits are kept for the next step, outward tracking. In this step, these tracks are used for the outward seed and track finding procedure. The tracks are built again from their innermost hit, assumed to be $e^+e^-$ pair crossing point, and the ECAL basic cluster positions.

Since a photon conversion features a pair of oppositely charged tracks originating from the same point where the conversion happens (called conversion vertex). Thus, the angular separations between two tracks at the conversion vertex in the trans-

verse plane ($\delta\phi$) and longitudinal plane ($\delta cot\theta$) are used for conversion identification. Requirement on $\chi^2$ of the vertex fit is needed to ensure the quality of the conversion finding. Figure 3.11 shows these variables in the 7 TeV data.

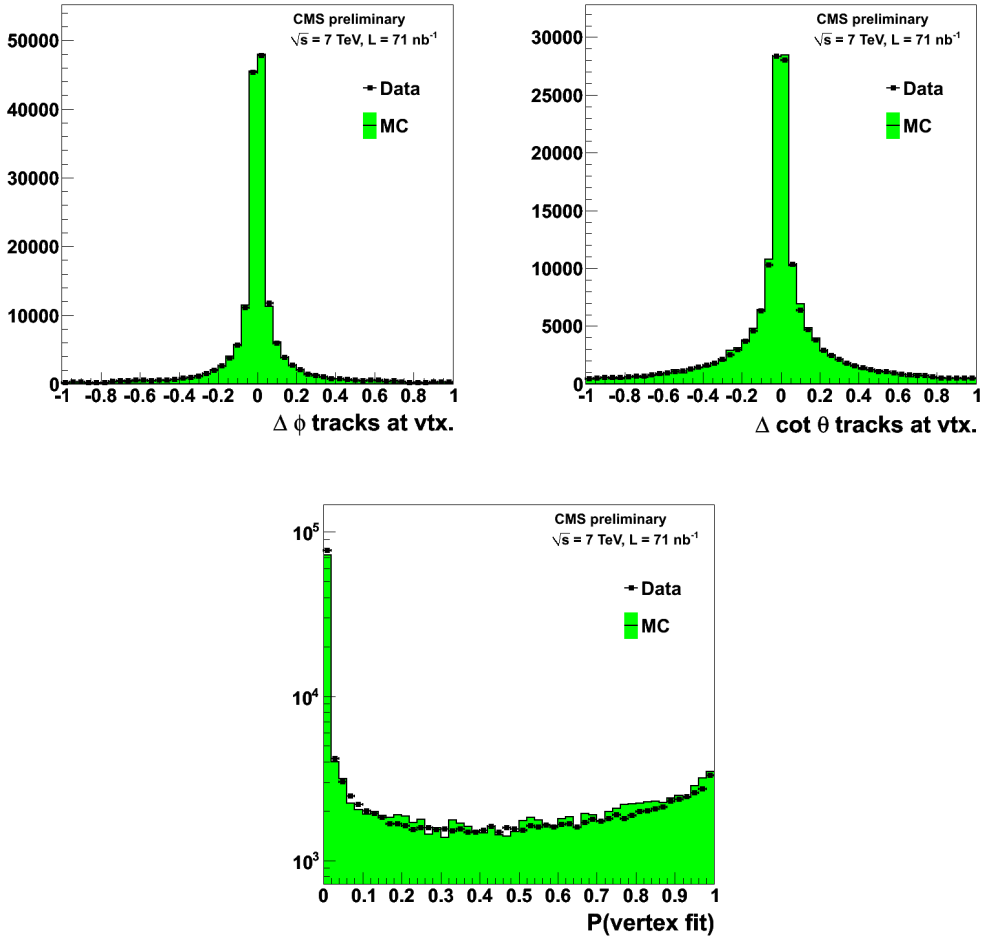


**Figure 3.11:** Conversion identification variables [15]

### 3.5.5 Electron

An electron candidate is a supercluster matched with a track. In contrast to photons, energy of electrons are measured in supercluster in order to recover bremsstrahlung enegy lost. Two complement tracking algorithms in the track seeding generation are

used ECAL driven [55] and tracker driven. The ECAL driven methods is optimized for an isolated electron with $p_T$ in the range of electron from Z and W decays and down to ∼5 GeV. The tracker driven method performs better for low $p_T$ electrons and electrons inside jets. The track reconstruction uses Gaussian sum filter (GSF) algorithm which is optimized for electron tracks with long non Gaussian tail in the energy loss distribution [56]. The GSF algorithm is built on a specific modeling of the electron energy loss and fitted (weighted sum of Gaussian distributions). Thus, it can adapt the change of curvature of the electron tracks and measures the track momentum at both track ends without a bias. Electrons are classified in the following classes [55]:

- "golden": a collection of low bremssstrahlung electrons with a reconstructed track well matching a supercluster
  - a supercluster formed by a single cluster (i.e. without observed bremsstrahlung sub-cluster)
  - $E/p$ >0.9
  - $f_{brem}$ <0.5
- "big brem": electrons with high bremsstrahlung fraction but no evidence of energy loss effects:
  - a supercluster formed by a single cluster,
  - $E/p$ >0.9
  - $f_{brem}$ >0.5
- "showering", or electrons with energy pattern highly affected by bremsstrahlung losses:

– a supercluster formed by a single cluster not falling into the "golden" or "big brem" classes, or a supercluster formed by several subclusters.

$f_{brem} = (p_{in} - p_{out})/p_{in}$ where $p_{in}$ and $p_{out}$ are the track momenta at the innermost and outermost points. Furthermore, there are "crack" electrons which have supercluster's starting crystal close to an $\eta$ boundary between ECAL modules, or between ECAL barrel and endcaps. The classification is used to improve electron momentum measurement. For a cut-based analysis, different cuts are designed for each electron class. The electron selection can be mostly based on a matching between a track and a supercluster, ratios between electron energy and momentum at innermost or outermost point of track. Shower shape and isolation variables are also used. Figure 3.12 shows the $p_T$ and $\eta$ distribution in minimum bias events at 7 TeV.

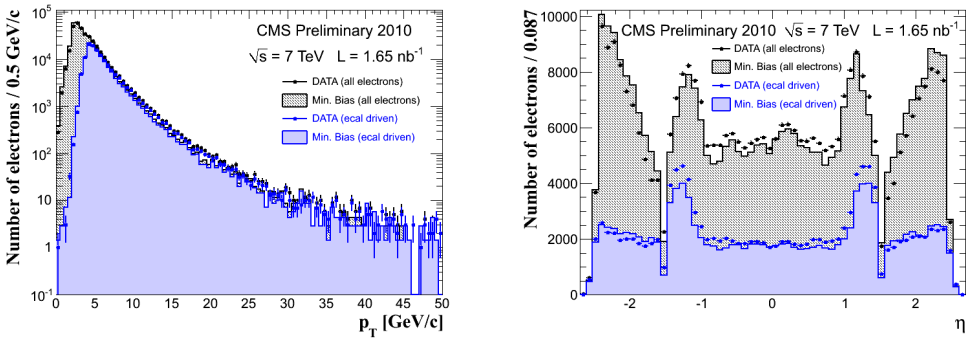


**Figure 3.12:** $p_T$ and $\eta$ distribution of electron [16]

# Chapter 4

# Analysis

The search for large extra dimensions in the diphoton channel are described in this chapter. We measure the invariant mass spectrum of photon pairs in data and look for an excess over the SM predictions (backgrounds) at high masses due to the production of gravitons decaying to two photons. The high mass region is called the signal region since the LED signatures, if they exist, present in this region. The main sources of backgrounds come from the SM diphoton, photon+jet and dijet processes. From the background studies at the signal region, the SM diphoton background is the most dominant background followed by the photon+jet background. The dijet process contributes a smallest fraction of the total background. The SM diphoton background is estimated in Monte Carlo simulation while photon+jet and dijet backgrounds are measured by data-driven methods.

This chapter starts with the description of the data and samples used in this analysis in Section 4.1. Next, we discuss about the optimization of kinematic cuts to obtain the best sensitivity for the LED signals in Section 4.2. The event selection, its

efficiency and the corresponding jet-faking-photon rate are described in Section 4.3, Section 4.5 and Section 4.6, respectively. Finally, the method of background estimation are discussed in Section 4.7.

## 4.1 Data and Monte Carlo Samples

About 36 $pb^{-1}$ of data collected in 2010 runs are used in this analysis. The reconstruction software is updated regularly during the data collection for latest improvement and up-to-date running conditions. After the period of data taking (often between technical stop of the LHC), collected data are reprocessed in order to bring them to the same reconstruction release which is the latest and greatest. The data quality is guaranteed by applying a data certification file in the JSON format (Java Script Object Notation) on top of the data processing. A JSON file includes only good luminosity sections, where the LHC machine and the CMS detector are in good operation, giving high quality collision data. The following data sets are used:

- EG (Egamma) data set: `/EG/Run2010A-Nov4ReReco_v1/RECO`; lumi: 3.18 $pb^{-1}$, run range: 136035-144114
- Photon data set: `/Photon/Run2010B-Nov4ReReco_v1/RECO`; lumi: 32.96 $pb^{-1}$, run range: 146428-149294

These data set are first collected in two data taking periods, Run2010A and Run2010B. After that they are reprocessed in `CMSSW_3_8_6` release in November, 2010. The EG data set comes from the HLT paths triggering on high transverse momentum electromagnetic objects (supperclusters). In Run2010B, the luminosity

is increased significantly, the photon data set are selected by tighter HLT photon filters to enrich well-defined photon candidates while the rate is maintained.

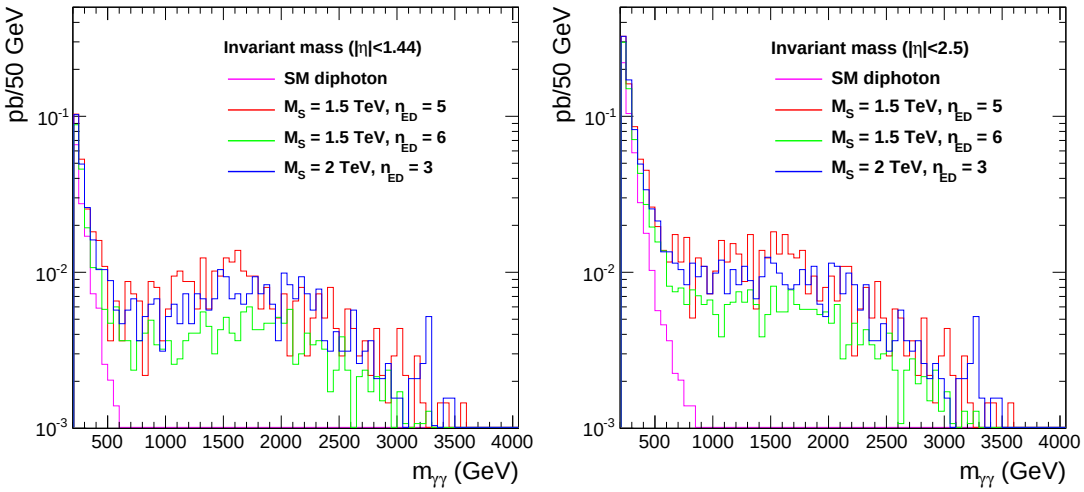


**Figure 4.1:** Invariant mass distributions of the SM diphotons and some ADD signals. The invariant masses are plotted for EB (left) and EB+EE (right) regions

The general purpose generator PYTHIA [57] is used to generate samples for SM diphoton study. PYTHIA contains a library of hard processes and models for initial- and nal-state parton showers, multiple parton-parton interactions, beam remnants, string fragmentation and particle decays [58]. Both Born and Box process are included in the sample generation. In order to increase the statistic at high $\widehat{p}_T$ phase space, where $\widehat{p}_T$ is the transverse momentum of the hard scattering, the event generation is done in separate sub $\widehat{p}_T$ phase spaces. Below are the Born and Box samples generated in different sub $\widehat{p}_T$ phase spaces from 10 to infinity. The $\sigma$ stands for the cross section.

- /DiPhotonBorn_Pt10to25/Summer10-START36_V9_S09-v1/GEN-SIM-RECODEBUG, $\widehat{p}_T$ = 10-25 GeV, $\sigma$ = 236.4 pb
- /DiPhotonBorn_Pt25to250/Summer10-START36_V9_S09-v1/GEN-SIM-RECODEBUG, $\widehat{p}_T$ = 25-250 GeV, $\sigma$ = 22.37 pb

- /DiPhotonBorn_Pt25toInf/Summer10-START36_V9_S09-v1/GEN-SIM-RECODEBUG, $\widehat{p}_T$ = 25-$\infty$ GeV, $\sigma = 8.072 \times 10^{-3}$ pb
- /DiPhotonBox_Pt10to25/Summer10-START36_V9_S09-v1/GEN-SIM-RECODEBUG, $\widehat{p}_T$ = 10-25 GeV, $\sigma = 358.2$ pb
- /DiPhotonBox_Pt25to250/Summer10-START36_V9_S09-v1/GEN-SIM-RECODEBUG, $\widehat{p}_T$ = 25-250 GeV, $\sigma = 12.37$ pb
- /DiPhotonBox_Pt250toInf/Summer10-START36_V9_S09-v1/GEN-SIM-RECODEBUG, $\widehat{p}_T$ = 250-$\infty$ GeV, $\sigma = 2.08 \times 10^{-4}$ pb

We also use PYTHIA to generate photon+jet samples. These samples are used in the background estimation.

- /PhotonJet_Pt30/Summer10-START36_V9_S09-v1/GEN-SIM-RECODEBUG
  cross section: $2.007 \times 10^4$ pb$^{-1}$
- /PhotonJet_Pt80/Summer10-START36_V9_S09-v1/GEN-SIM-RECODEBUG
  cross section: 556.5 pb
- /PhotonJet_Pt170/Summer10-START36_V9_S09-v1/GEN-SIM-RECODEBUG
  cross section: 24.37 pb
- /PhotonJet_Pt300/Summer10-START36_V9_S09-v1/GEN-SIM-RECODEBUG
  cross section: 1.636 pb

We use the SHERPA generator version 1.1.2 to generate the ADD signal samples. *SHERPA* implements the ADD model based on the helicity formalism of spin-2 particles [59]. In order to take into account for the interference between SM diphoton production and ED diphoton effects, Sherpa generates both processes together. We

generate several signal samples with various values of $n_E D$ and $M_S$. The cross sections of the pure ED effect after subtracting the SM term are also shown in Table 4.1. We also generate a sample with $M_S = 100$ TeV, which effectively turns off virtual graviton effects, while retaining SM diphoton production.

| | Positive Interference (HLZ) | | Negative Interference (Hewett) | |
|---|---|---|---|---|
| Sample | $\sigma$ (pb) | $\sigma \times \mathcal{A}$ (pb) | $\sigma$ (pb) | $\sigma \times \mathcal{A}$ (pb) |
| $M_S = 1.2$ TeV, $n_{\mathrm{ED}} = 5$ | 7.31 | 3.19 | — | — |
| $M_S = 1.5$ TeV, $n_{\mathrm{ED}} = 2$ | 3.32 | $7.14 \times 10^{-1}$ | 1.90 | $3.04 \times 10^{-1}$ |
| $M_S = 1.5$ TeV, $n_{\mathrm{ED}} = 5$ | 2.16 | $3.34 \times 10^{-1}$ | | |
| $M_S = 1.5$ TeV, $n_{\mathrm{ED}} = 6$ | 1.69 | $1.82 \times 10^{-1}$ | | |
| $M_S = 1.5$ TeV, $n_{\mathrm{ED}} = 7$ | 1.47 | $1.02 \times 10^{-1}$ | | |
| $M_S = 2$ TeV, $n_{\mathrm{ED}} = 2$ | 1.35 | $6.06 \times 10^{-2}$ | 1.12 | $2.79 \times 10^{-2}$ |
| $M_S = 2$ TeV, $n_{\mathrm{ED}} = 3$ | 2.05 | $2.98 \times 10^{-1}$ | | |
| $M_S = 2$ TeV, $n_{\mathrm{ED}} = 4$ | 1.32 | $6.78 \times 10^{-2}$ | | |
| $M_S = 2$ TeV, $n_{\mathrm{ED}} = 7$ | 1.11 | $1.36 \times 10^{-2}$ | | |
| $M_S = 2.5$ TeV, $n_{\mathrm{ED}} = 2$ | 1.15 | $2.02 \times 10^{-2}$ | 1.06 | $1.07 \times 10^{-2}$ |
| $M_S = 2.5$ TeV, $n_{\mathrm{ED}} = 3$ | 1.24 | $4.54 \times 10^{-2}$ | | |
| $M_S = 2.5$ TeV, $n_{\mathrm{ED}} = 4$ | 1.11 | $1.52 \times 10^{-2}$ | | |
| $M_S = 2.5$ TeV, $n_{\mathrm{ED}} = 7$ | 1.07 | $1.91 \times 10^{-3}$ | | |
| $M_S = 3$ TeV, $n_{\mathrm{ED}} = 2$ | 1.10 | $7.75 \times 10^{-3}$ | 1.05 | $7.04 \times 10^{-3}$ |

**Table 4.1:** Total cross section and cross section × acceptance for different samples. Cross sections include SM diphoton production in addition to ADD phenomena. The acceptance criteria are two generator-level photons with $E_T > 30$ GeV and $|\eta| < 1.442$ that form an invariant mass $M_{\gamma\gamma} > 500$ GeV. The first set of cross sections (columns two and three) have positive interference between SM and ADD signals, while the second set (columns four and five) have negative interference. The second set is used in the Hewett convention of virtual graviton production. No NLO $K$-factor is applied.

## 4.2 Signal Optimization

We optimize our selection criteria to minimize the expected 95% confidence level limit on the cross section for the ADD model with parameters close to the expected sensitivity. The process of calculating the expected limit is described in detail in Section 5.3. For the optimization, we ignore any systematic uncertainties. We opti-

mize based on an estimation of the diphoton rate from MC and the jet background from data.

We optimize on two variables: the invariant mass of the photon pairs, and the maximum allowed $|\eta|$ of the individual photons. Virtual KK graviton production will evince itself as a contiuum spectrum above the expected SM background at high invariant mass. The signal is also more central than the SM (see Figure 4.2). To find the best choice of selection values, we first fix the invariant mass requirement at $M_{\gamma\gamma} > 400$ GeV, and then find the optimal $|\eta|$ requirement. Once this is found, we fix the $|\eta|$ requirement, and measure the optimal $M_{\gamma\gamma}$ cut. This iterative process helps us converge on an optimal point without needing to optimize on both variables simultaneously.

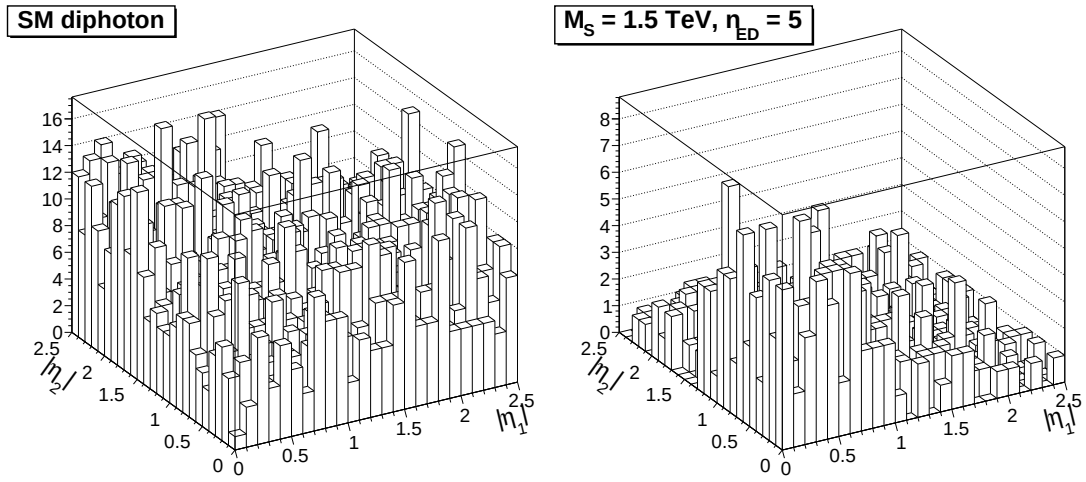


**Figure 4.2:** Pseudo rapidity distributions of two photons for SM diphoton (left) and ADD signals with $M_S = 1.5$ TeV $n_{ED} = 5$

Figure 4.3 shows both steps of optimization process. The plot on the left is the expected 95% confidence level limit on the signal cross section as a function of $|\eta|$ with $M_{\gamma\gamma} > 400$ GeV for a variety of choices for $M_S$ and the number of ED. The normalization is arbitrary since we are looking only for local minima. We choose

$|\eta| < 1.442$, since this conveniently corresponds to both the approximate location of the optimal cut point and the location of the gap between the ECAL barrel and endcap.

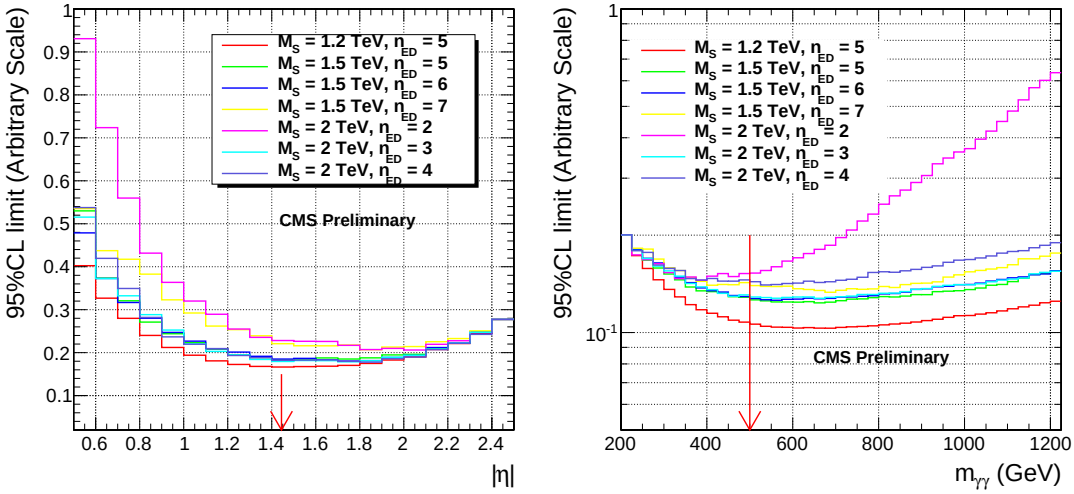


**Figure 4.3:** Expected 95% limit on the cross section for various ED models. Left: the limit as a function of $|\eta|$ with $M_{\gamma\gamma} > 600$ GeV. Right: the limit as a function of $M_{\gamma\gamma}$ with $|\eta| < 1.442$.

After the optimum $|\eta|$ cut has been chosen, we focus on the invariant mass threshold. This is shown in the right pane in Figure 4.3. Based on this plot, we choose to require $M_{\gamma\gamma} > 500$ GeV, as this is the optimal point for much of the parameter space.

## 4.3 Event Selection

The final goal of the event selection is to select a high-purity diphoton candidate sample without loosing hypothetical new physics signals. At first, the events are selected by the CMS 2-level trigger systems described in Section 2.2.6. The generic double-photon trigger paths in Table 4.2 are used. At least one good vertex within $|z| < 24$ cm and $d_0 < 2$ cm of the detector center is required, where z is the z-coordinate of

the vertex and $d_0$ is the distance from the vertex to the beam line. The next step is to select events containing two high-transverse-momentum photons. Table 4.3 lists the kinematic and the photon identification cuts. The $\eta$ cut is equivalent to restricting two photons to the ECAL barrel. As discussed in Section 4.2, this choice is a good compromise between the search sensitivity and the need to understand complicated backgrounds in the ECAL endcap.

| Run range | Trigger name | Threshold (GeV) |
|---|---|---|
| 136033-141881 | $HLT\_DoublePhoton10\_L1R$ | 10 |
| 141882-144114 | $HLT\_DoublePhoton15\_L1R$ | 15 |
| 144115-148058 | $HLT\_DoublePhoton17\_L1R$ | 17 |
| 148059-149294 | $HLT\_DoublePhoton22\_L1R\_v1$ | 22 |

**Table 4.2:** HLT trigger path

| Cuts | Tight value |
|---|---|
| $E_T$ | $< 30$ GeV |
| $\|\eta\|$ | $< 1.4442$ |
| EcalIso | $< 4.2 + 0.006 \cdot p_T$ GeV |
| HcalIso | $< 2.2 + 0.0025 \cdot p_T$ GeV |
| TrkIso | $< 2 + 0.001 \cdot p_T$ GeV |
| Pixel seed veto | false |
| $\sigma_{i\eta i\eta}$ | 0.013 |

**Table 4.3:** Photon selection. The $\eta$ cut is defined from the sensitivity optimization presented in Section 4.2

## 4.4 Anomalous energy deposit cleaning

Anomalous energy deposits are isolated high energy deposits observed in ECAL barrel due to direct ionization of the avalanche photodiode (APD) sensitive volumes by highly ionizing particles, mainly protons and heavy ions, produced during proton-proton collisions [17]. Because, these energy deposits are often observed in a single ECAL crystal, they are called "spikes". They are found at the rate of $\sim 1$ in $10^3$

minimum bias events. This rate is scaled with $\sqrt{s}$ consistence with the increase in charged particle multiplicity.

The rejection of those spikes are based on the topological and timing characteristic. A spike appear as a high energy deposit in a single crystal surrounded by quiet adjacent crystals. The "Swiss Cross" variable (S) defined as $1 - E_4/E_1$, where $E_1$ is the energy of the seed crystal (a crystal with highest energy in a cluster of a photon) and $E_4$ is the total energy of four crystal adjacent to the seed crystal, are used in spike cleaning. A cut at S $< 0.95$ reject 99.2% spikes with $E_T > 10$ GeV [17].

A genuine signal pulse from a photon is the convolution of the time profile of light emission from the lead tungstate crystals (80% of light emitted in 25 ns) and the response of the front-end electronics (shaping time $\tau \sim 40$ ns). In contrast, the signal pulse from a spike contains only the electronic shaping time since the spike energy deposit happens inside the APD. This difference in shape produces a bias in the measured time of the signal pulse when the anomalous energy deposits are reconstructed with the expected pulse shape for scintillation light [17]. A pulse is declared out-of-time if the difference between the measured and expected time is greater than 5 standard deviations [17].

Figure 4.4 shows the Swiss Cross variable and the signal timing distributions of photon. A pronounced peak $\sim 1$ is seen in Swiss Cross variable distribution for data. The timing distribution shows many out-of-time photons. Both the Swiss Cross cut and the timing cut are applied when processing data to reject automatically spike photons.

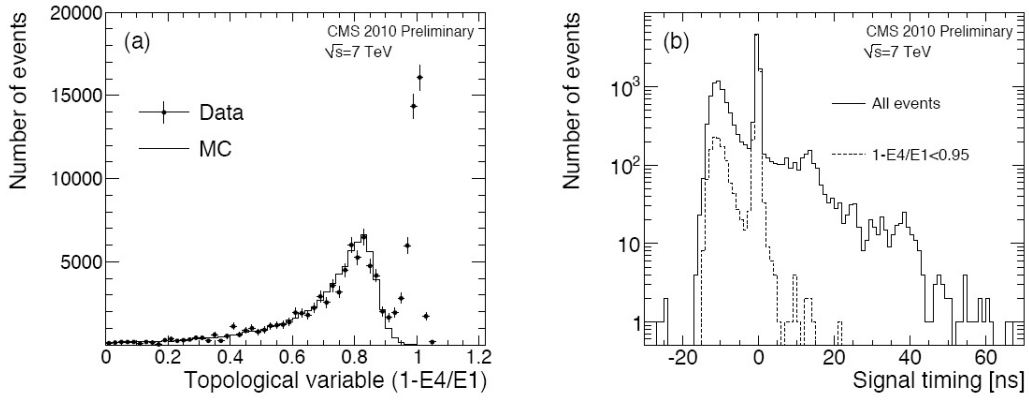


**Figure 4.4:** (a) Distribution of the Swiss Cross topological variable (1-$E_4/E_1$) for the highest energy deposit each event for data and simulation ($\sqrt{s}$ = 7 TeV); (b) Reconstructed time corresponding to the maximum of the signal pulse for the highest energy deposit in each event [17]

## 4.5 Photon efficiency

The photon efficiency is measured using the MC photon+jet samples. A generator-level photon is spatially matched to a reconstructed photon. If a reconstructed photon is found, the photon identification efficiency is calculated. The MC matching is necessarily since a photon can be reconstructed from a electromagnetic fluctuation of a jet. Figure 4.5 shows the efficiency versus photon $p_T$ and $\eta$ in MC. The combined efficiency is flat in $p_T$ and $\eta$ and central at 90%. A 2% systematic uncertainty is assigned to account for a small variation of the efficiency. In order to correct for the difference between efficiency in MC and data, a scale factor is derived. Because of the similarity between photons and electrons, this scale factor for photons is similar to that of electron which is derived in $Z \rightarrow e^+e^-$ events using the tag-and-probe technique. The scale factor value is 1.010±0.012 with the uncertainty covering the difference between photons and electrons [60].

Another piece of the photon efficiency is the efficiency of the pixel seed veto which is $96.6 \pm 0.5(syst)\%$. This quantity is also estimated in MC and its uncertainty is obtained by comparing different geometry configurations of the beam pipe and the

pixel detector [61]. The total single photon efficiency for the selection in Table 4.3 is (87.8±2.3)% which can be turned into the diphoton reconstruction and identification efficiency of (77.1±4.5)%.

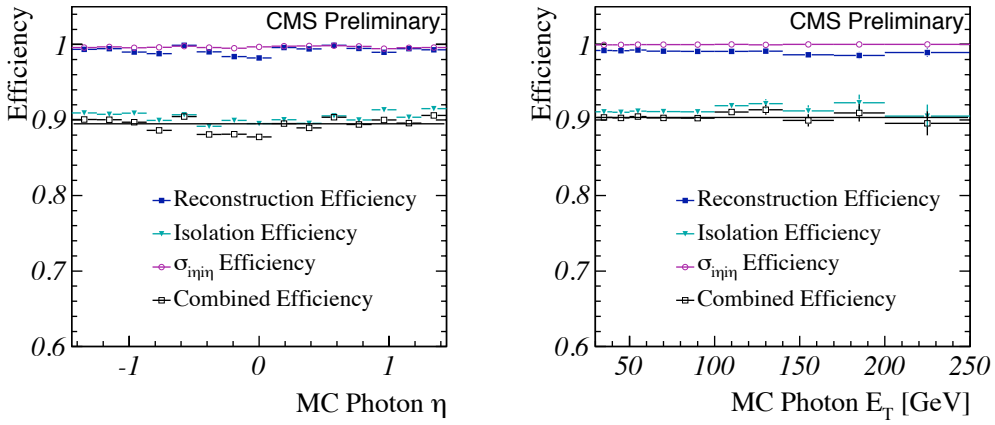


**Figure 4.5:** Reconstruction, $\sigma_{i\eta i\eta}$ cut, isolation, and combined efficiency as a function of $p_T$ and $\eta$.

## 4.6 Jet-faking-photon rate

A jet can misidentified as a "fake photon", especially when most of its energy is carried by electromagnetic decay particles, for example $\pi_0$. Although jet-faking-photon rate (or photon fake rate for short) is small ($\sim 10^{-4}$), the contribution of the backgrounds coming from the SM processes associated with jets in the final state (e.g., dijets and photon+jets) to photon analysis can be significant due to the high cross section of those processes. In this section, a method to estimate the photon fake rate is described. The photon fake rate is derived from a photon data set collected by single photon trigger paths which contain very loose photons. In this data set, the number of photons passing the tight selection in Table 4.3, $N_T^{fake}$ and the number of photons passing the loose photon selection $N_L^{fake}$ are found. The loose photon

selection is defined as:

$E_T < 30$ GeV

$|\eta| < 1.4442$

$EcalIso < min(5 \times (4.2 + 0.006 \times p_T), 0.2 \times p_T)$

$HcalIso < min(5 \times (2.2 + 0.0025 \times p_T), 0.2 \times p_T)$

$TrkIso < min(5 \times (3.5 + 0.001 \times p_T), 0.2 \times p_T)$

AND

{

$EcalIso > (4.2 + 0.006 \times p_T) OR$

$HcalIso > (2.2 + 0.0025 \times p_T) OR$

$TrkIso > (3.5 + 0.001 \times p_T) OR$

$\sigma_{i\eta i\eta} > 0.013$

} where $p_T$ is in GeV. The photon fake rate is defined as:

$$f_\gamma = \frac{N_T^{fake}}{N_L^{fake}}. \tag{4.1}$$

The denominator photon selection contains an inverted tight photon ID cut which is needed to reduce the contamination from direct photons. It can be seen that the fake rate is not exactly the probability of a fake photon to be recognized as a tight photon which is defined as:

$$p_\gamma = \frac{N_T^{fake}}{N_T^{fake} + N_L^{fake}} \tag{4.2}$$

However, those are related by

$$f_\gamma = \frac{p_\gamma}{1 - p_\gamma} \tag{4.3}$$

The tight photons observed in the data, $N_T^{obs}$ include both $N_T^{fake}$, which originated from jets and direct photons or real photons mostly from photon+jets processes. The photon purity, P, which is the fraction of direct photons in $N_T^{obs}$ can be as high

as 70% at $p_T$ ∼80 GeV. The equation Eq. 4.1 is rewritten as:

$$f_\gamma = \frac{N_T^{obs} \times (1 - P)}{N_L^{fake}} \tag{4.4}$$

The contribution of genuine photons to the denominator in Eq. 4.4 is negligible due to the inverted tight photon ID cut applied.

### 4.6.1 Photon purity

The photon purity is the fraction of prompt photons in the sample of interest. Here, the sample of interest contains the tight photons selected by the tight selection in Section 4.3. The template method is used. The prompt photon templates (the signal templates), and the fake photon template (the background templates) are provided as inputs. A binned likelihood fit is perform to find the best fit of those templates to data.

The shower shape template, $\sigma_{i\eta i\eta}$, is powerful in the signal-background separation. Therefore, the shower shape method is chosen to get the central values of the purity. Other template methods, the isolation sum and the conversion methods, are also considered as cross-checks and discussed later in this section. The prompt photon templates can be obtained from the photons associated with $W$ or $Z$ bosons in which the fake photons are reduced significantly by the $W$ or $Z$ selection. With insufficient events of those processes, we derive the real photon templates from Monte Carlo (MC) photon+jet samples. The background templates are derived in a background-enriched region given by inverting the track isolation requirement $2 + 0.001 \times p_T < trackisolation < 4$ GeV. There may be correlation between the shower shape variable and the track isolation cuts used to define the background-enriched region. This

correlation can affect the correctness in modeling the background templates at the signal region. The fit is performed by the `TFractionFitter` method of `ROOT`. The `TFractionFitter` is a standard likelihood fit using Poisson statistics. The results of the fit are presented in Figure 4.6.

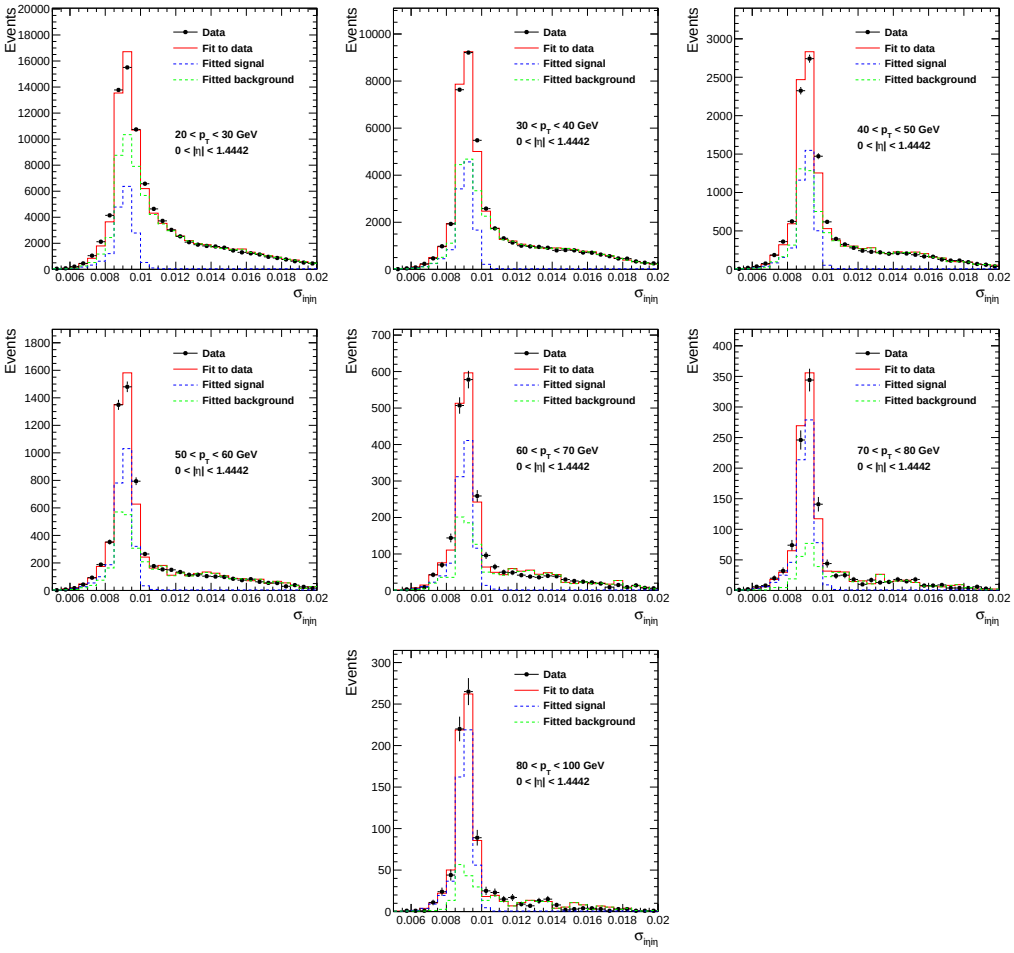


**Figure 4.6:** $\sigma_{i\eta i\eta}$ template fit.

The sum of photon isolation is defined as $Iso = Iso_{Ecal} + Iso_{Hcal} + Iso_{Trk}$. Here $Iso_{Ecal}, Iso_{Hcal}, Iso_{Trk}$ are the isolation variables in Ecal, Hcal and tracker, respectively. This variable is also good in signal-background separation and can be used in the template fitting. The signal templates are derived in MC while the background templates are obtained from a nearby side-band region, $0.011 < \sigma_{i\eta i\eta} <$

0.013. The main drawback of this method is that the isolation is very sensitive to the pile-up effects and the sample used in the purity calculation is different from the sample of interest selected by tight selection. The pile-up effects are not well-simulated in MC so the difference between a MC signal template and a true data template can be significant. The later drawback implies that the calculated purity and the purity in the sample of interest may not be the same. Figure 4.7 shows the fit results.

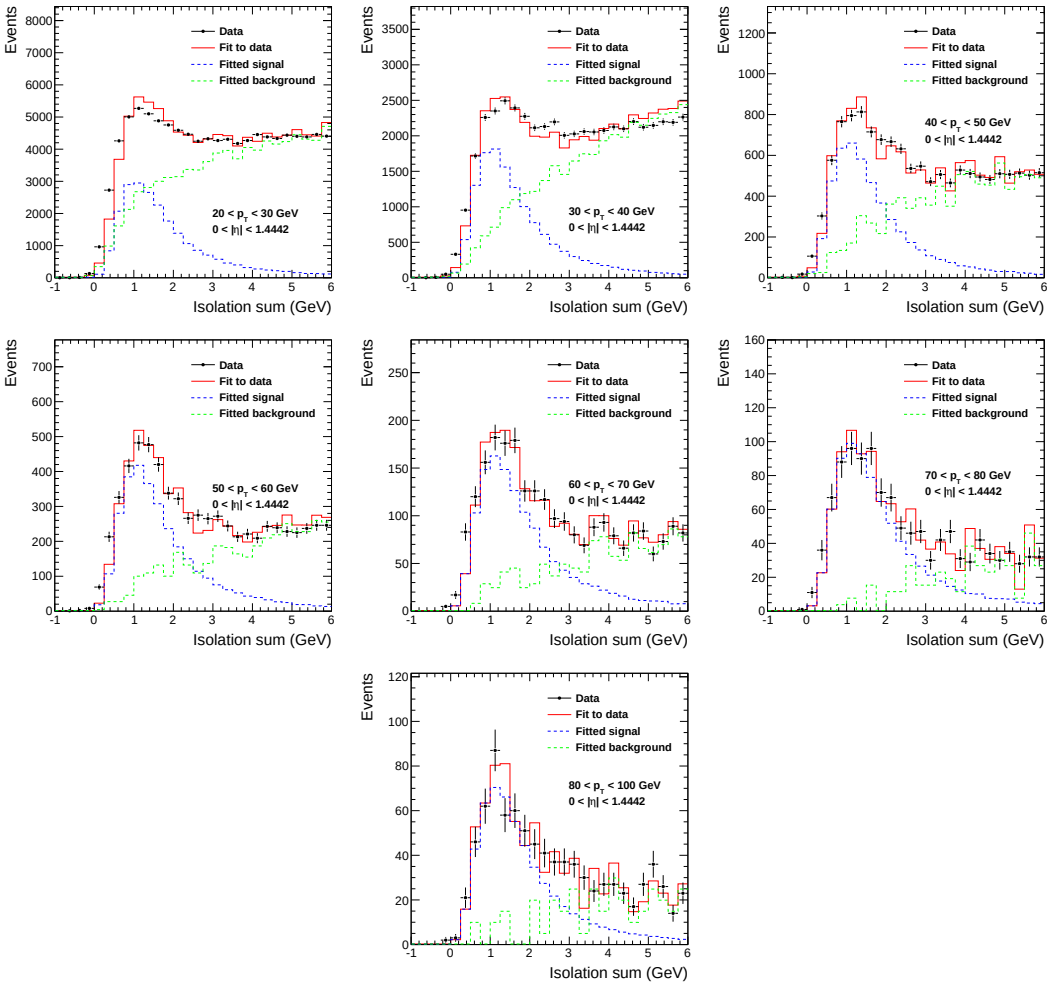


**Figure 4.7:** Isolation sum template fit.

Finally, our final method is to use converted photons. Two photons are selected by requiring that two, oppositely charged tracks associated with corresponding elec-

tromagnetic clusters form a conversion vertex: $|\Delta\cot(\theta)| < 0.05$ and $|\Delta\phi_{vtx}| < 0.1$. These photons are required to pass the tight selection. A side-band region of $0.011 < \sigma_{i\eta i\eta} < 0.013$ is used to get the background templates. Figure 4.8 shows the result of the conversion fits.

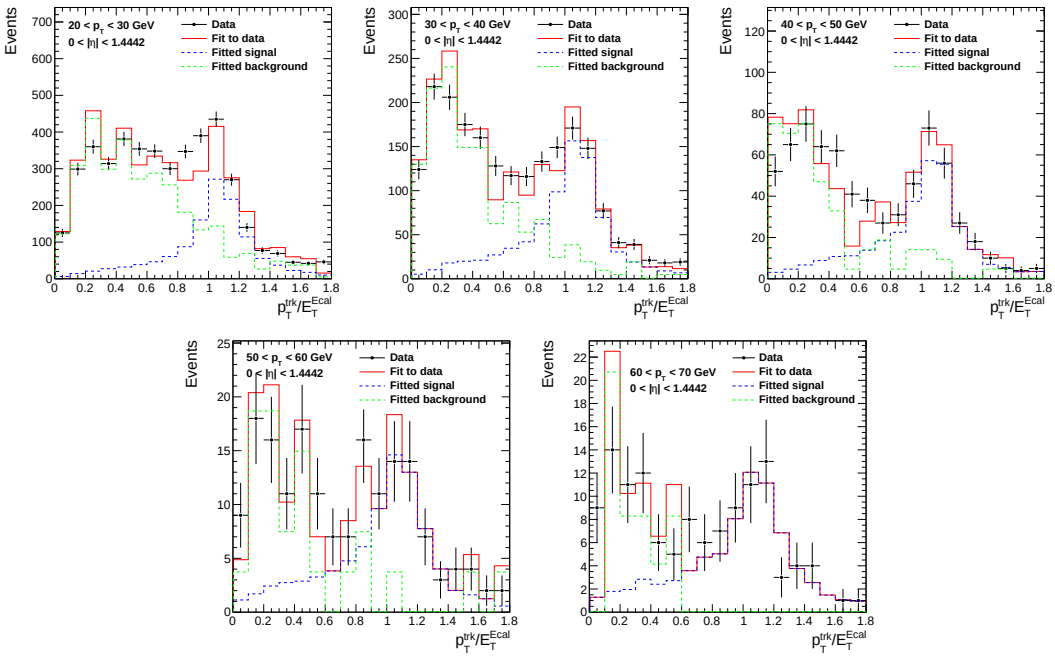


**Figure 4.8:** Conversion template fit.

## 4.6.2 Corrected fake rate

By correcting the measured fake rate for the purity as a function of photon $E_T$, we get the rates shown in Figure 4.9 for each of the template methods. Table 4.4 shows those rates in numbers. We see that the fake rates from the isolation and the conversion methods are within 20% relative with respect to the central values from the $\sigma_{i\eta i\eta}$ method.

| $E_T$ bin (GeV) | Shower shape | Isolation sum | Conversion |
|---|---|---|---|
| 20-30 | $0.532 \pm 0.009$ | $0.491 \pm 0.008$ | $0.535 \pm 0.027$ |
| 30-40 | $0.183 \pm 0.003$ | $0.177 \pm 0.003$ | $0.205 \pm 0.010$ |
| 40-50 | $0.128 \pm 0.003$ | $0.114 \pm 0.003$ | $0.140 \pm 0.011$ |
| 50-60 | $0.076 \pm 0.002$ | $0.067 \pm 0.002$ | $0.097 \pm 0.013$ |
| 60-70 | $0.056 \pm 0.002$ | $0.044 \pm 0.002$ | $0.068 \pm 0.009$ |
| 70-80 | $0.033 \pm 0.002$ | $0.027 \pm 0.001$ | - |
| 80-100 | $0.030 \pm 0.002$ | $0.030 \pm 0.002$ | - |

**Table 4.4:** Fake rates from shower shape, isolation sum and conversion methods

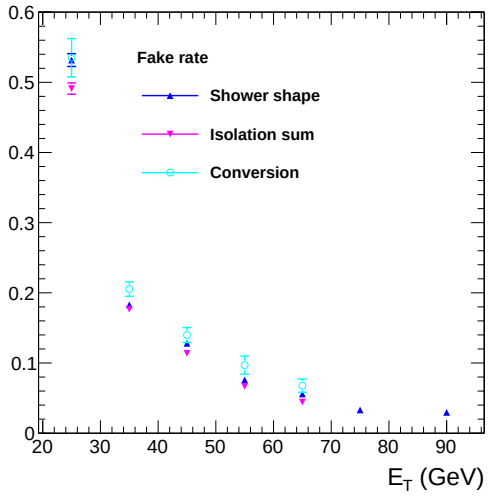


**Figure 4.9:** Photon fake rate using various methods of correcting for the real photon contamiation.

### 4.6.3 Fake rate and trigger

The single photon triggers are used to get the results in Section 4.6.2. This section discusses the choice of triggers. The non-isolated HLT triggers in which there is no any isolation requirement applied to photon trigger objects are chosen. The fake rate for each trigger with thresholds at 30, 50 and 70 GeV are shown in Figure 4.10. It can be seen that the fake rate is decreased below the thresholds and above the trigger thresholds all fake rates are in good agreement. Therefore, the 30, 50 and 70 GeV triggers are used for estimating the fake rate in $p_T$ range 30-50, 50-70 and above 70, respectively. The fake rates are also derived from the samples selected by

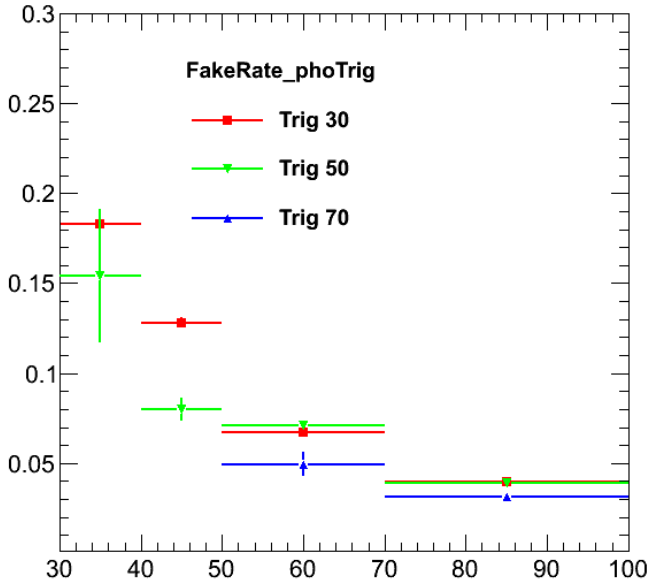


**Figure 4.10:** Photon fake rates from photon (red), muon (blue) and jet (green) triggers and their ratios to the best fit function.

jet or muon triggers. There are a small discrepancies between the results from those triggers. The fake rates of different triggers are then combined in a common fit by a function of $E_T$:

$$p_0 + \frac{p_1}{x^{p_2}} \tag{4.5}$$

The fit results are shown in Figure 4.11. The coefficients found from a best fit are:

$$p_0 = 0.01598, p_1 = 2431.92, p_2 = 2.67771. \tag{4.6}$$

Figure 4.11 also represents the ratio of observed fake rates and the best fit function of combined fake rates. From that, a 20% systematic error is assigned to cover the variation of observed fake rates.

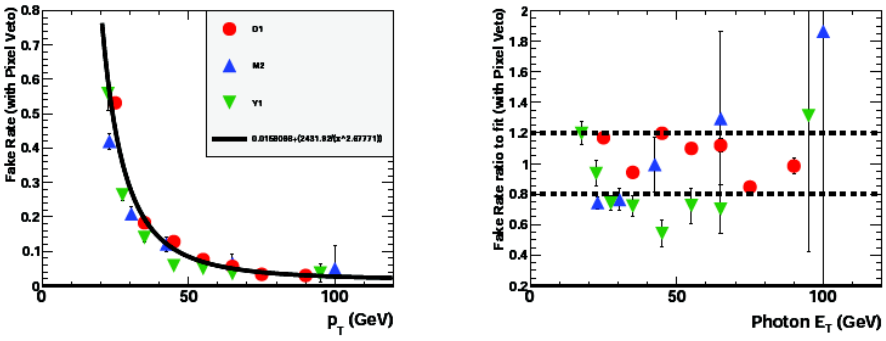


**Figure 4.11:** Photon fake rates from photon (red), muon (blue) and jet (green) triggers and their ratios to the best fit function.

## 4.7 Backgrounds

The main sources of backgrounds come from the SM diphoton production, so-called diphoton background, and the QCD processes with jets in the final states (dijets, photon+jets), so-called QCD background. The SM diphoton background is irreducible since the events always pass the photon selection and contribute significant to the total background especially at the signal region (the high end of the diphoton invariant mass spectrum). This type of background is estimated in MC and described in Section 4.7.1. The QCD background can be estimated in data-driven manner using the photon fake rate, the rate at which a jet fakes as a photon. This background is less important than the diphoton background in the signal region given the small photon fake rate ($10^{-4}$). The detail is at Section 4.7.2.

### 4.7.1 SM diphotons

The SM diphoton background is estimated in MC using PYTHIA generator and the full detector simulation by GEANT4. Both contributions from Born and Box processes are taken into account. Since these are the tree-level LO contributions,

the K-factor, which is the ratio between LO and NLO cross sections, is applied as a scale factor to the diphoton background prediction from PYTHIA. In this analysis, we apply a conservative K-factor of 1.3 used by Tevatron experiments. In principle, K-factor depends on the center-of-mass energy of hadron-hadron collisions and the invariant mass of the diphotons.

We use a dedicated program for diphoton cross section calculation, called DIPHOX [62], to study the K-factor of pp collision at 7 TeV. All the LO and NLO diagrams of direct and fragmentation processes described in Section 4.5 are implemented in DIPHOX. In order to be consistent with photon selection, we limit the $\eta$ range within $|\eta| < 1.4442$. Table 4.5 summarizes the parameter setup. Figure 4.12 shows the LO and NLO cross sections and the K-factor as the functions of the diphoton invariant mass.

| Name | Value |
|---|---|
| PDF | CTEQ6 |
| Type of fragmentation functions | 402 |
| Initial state factorisation scale | 0.5 cm |
| Final state factorisation scale | 0.5 cm |
| Renormalization scale | 0.5 cm |
| $\|\eta\|$ | $< 1.4442$ |
| $p_T$ | $> 30$ GeV |
| Radius of isolation cone | 0.4 |

**Table 4.5:** Parameter setup in DIPHOX for cross section calculation

### 4.7.2 Dijet and photon+jet

Utilizing the photon fake rate, the dijet and photon+jet backgrounds (QCD background) can be estimated by the following method. The events with two photons are considered. Among the total number of those events, there are $N_{\gamma\gamma}$ events with two real photons, $N_{jj}$ with two fake photons and $N_{\gamma j}$ with one real and one fake photon.

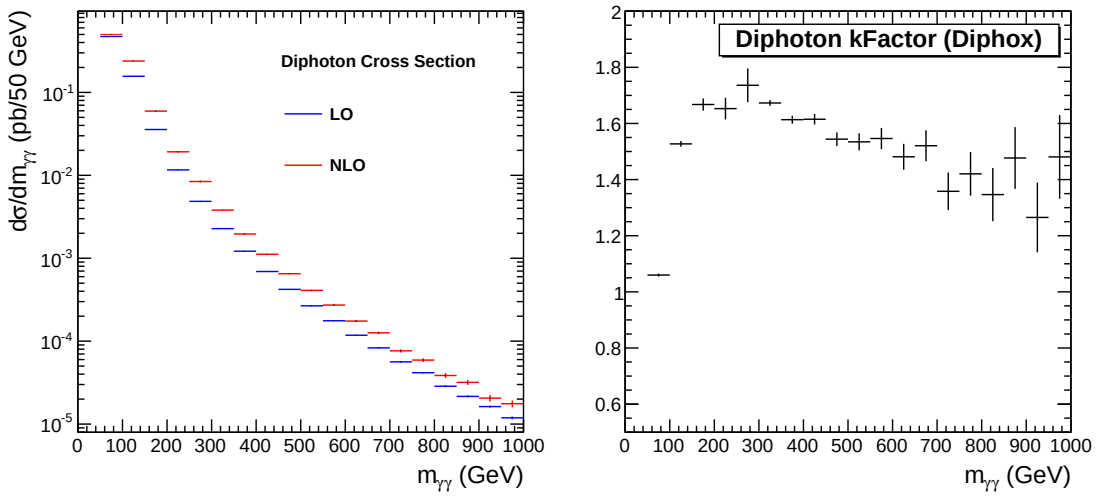


**Figure 4.12:** The diphoton cross sections (left) and the K-factor (right) from Diphox

If the transverse momenta of photons denoted as x and y, the numbers of events in each category are $N^{xy}_{\gamma\gamma}$, $N^{xy}_{jj}$, $N^{xy}_{\gamma j}$ and $N^{xy}_{j\gamma}$. The ordering of subscripts decides which photon has transverse momentum x or y. That is why two combinations for the case of one real and one fake photon are needed. An important thing is that those numbers of events are not known because the real and fake photons are mixed undistinguishable in data. What have been observed instead are the tight (denoted $T$) and the fakeable (denoted $F$) photons. Therefore, the observed diphoton events are $N^{xy}_{TT}$, $N^{xy}_{FF}$, $N^{xy}_{TF}$, $N^{xy}_{FT}$ corresponding to the number of diphoton events with two tight, two fakeable and one tight and one fakeable photons, respectively. Again, the ordering of the subscript indicates which photons has $E_T = x$ or $E_T = y$. Recalling that $p_x$ and $p_y$ are the probability of a photon identified as a tight photon, one can write these equations:

$$N^{xy}_{FF} = N^{xy}_{jj}(1-p_x)(1-p_y), \tag{4.7}$$

$$N^{xy}_{FT} = N^{xy}_{jj}(1-p_x)p_y + N^{xy}_{j\gamma}(1-p_x), \tag{4.8}$$

$$N^{xy}_{TF} = N^{xy}_{jj}p_x(1-p_y) + N^{xy}_{\gamma j}(1-p_y), \tag{4.9}$$

$$N^{xy}_{TT} = (N^{xy}_{jj}p_xp_y + (N^{xy}_{j\gamma}p_x + N^{xy}_{\gamma j}p_y) + (N^{xy}_{\gamma\gamma}). \tag{4.10}$$

Solving these equations, the number of diphoton events with two tight photons, which is the background to the analysis, can be expressed by observables and probability of identifying a tight photon:

$$\begin{aligned} N_{TT}^{xy} &= \left( N_{FF}^{xy} \frac{p_x p_y}{(1-p_x)(1-p_y)} \right) \\ &+ \left( -2N_{FF}^{xy} \frac{p_x p_y}{(1-p_x)(1-p_y)} + N_{FT}^{xy} \frac{p_x}{1-p_x} + N_{TF}^{xy} \frac{p_y}{1-p_y} \right) \\ &+ (N_{\gamma\gamma}^{xy}) \end{aligned}$$

The terms in parentheses correspond to the background contributions from di-jet, photon+jet and diphoton, respectively. Finally, using Eq. 4.3, we rewrite the expression in term of fake rate:

$$N_{TT}^{xy} = (N_{FF}^{xy} f_x f_y) + (-2N_{FF}^{xy} f_x f_y + N_{FT}^{xy} f_x + N_{TF}^{xy} f_y) + (N_{\gamma\gamma}^{xy}). \tag{4.11}$$

# Chapter 5

# Results and Conclusions

## 5.1 Data and background prediction

Figure 5.1 shows the diphoton invariant mass spectrum from data and background estimations. There is no excess of data events over the SM background estimations. Therefore, no signal of extra dimensions is found and the limit settings are proceeded. Table 5.1 presents the event counts in different diphoton invariant mass ranges. The uncertainties in the backgrounds come from 20% photon fake rate systematic uncertainty. In the signal region, $m_{gg} > 500$ GeV, the predicted SM background is $0.303 \pm 0.066$ and there is no event observed. The irreducible SM diphoton background is dominant in this signal region. The kinematic variables of the diphoton system are plotted in Figures 5.2 and 5.3. The background estimates agrees well with the number of observed events in those kinematic distributions.

**Table 5.1:** Data measurements and background expectations for reconstructed diphoton invariant mass ranges. Full systematic uncertainties have been included.

| Process | $60 < M_{\gamma\gamma} < 200$ GeV | $200 < M_{\gamma\gamma} < 500$ GeV | $500 < M_{\gamma\gamma}$ GeV |
|---|---|---|---|
| Dijets | $70 \pm 28$ | $0.5 \pm 0.2$ | $0.0009 \pm 0.0004$ |
| $\gamma$+Jets | $145 \pm 7$ | $2.3 \pm 0.3$ | $0.016 \pm 0.003$ |
| Diphotons | $150 \pm 35$ | $6.2 \pm 1.4$ | $0.286 \pm 0.066$ |
| Total Backgrounds | $365 \pm 49$ | $9.0 \pm 1.5$ | $0.303 \pm 0.066$ |
| Observed | 428 | 12 | 0 |

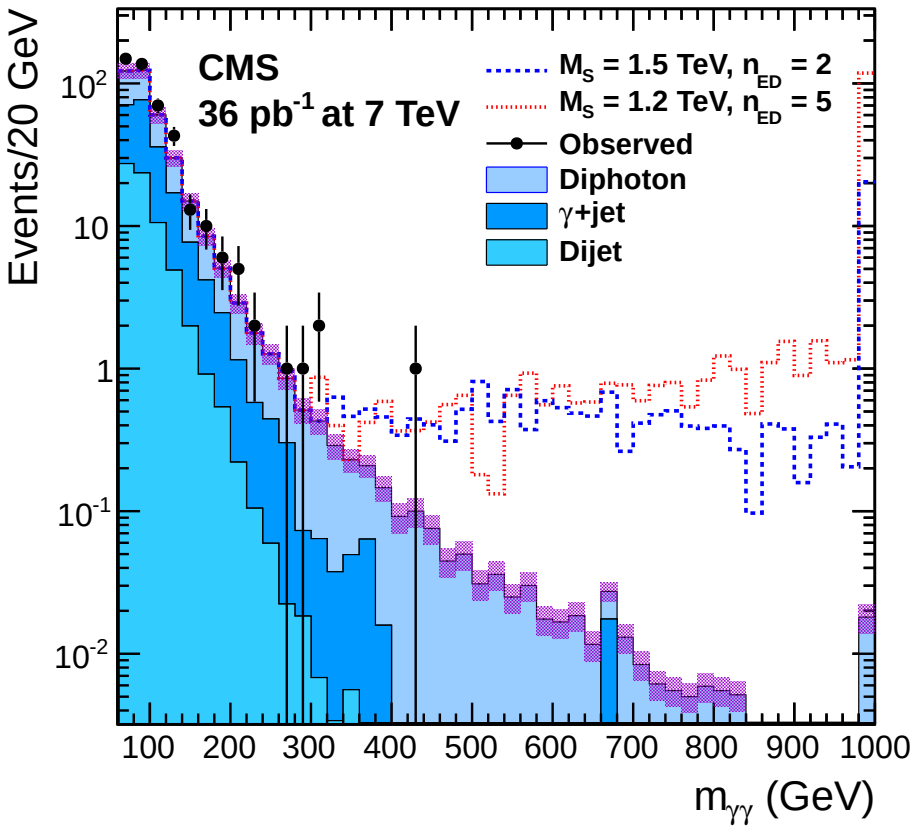


**Figure 5.1:** Data (points with error bars) and background expectations (filled solid histograms) as a function of the diphoton invariant mass. Photons are required to be isolated, with $E_T > 30$ GeV and $|\eta| < 1.4442$. Also shown with dashed lines the signal for two sets of model parameters.

## 5.2 Uncertainty

Table 5.2 summarizes the uncertainty of the analysis. The signal efficiency and signal K-factor uncertainty are described in Section 4.5 and Section 4.7.1. The uncertainty

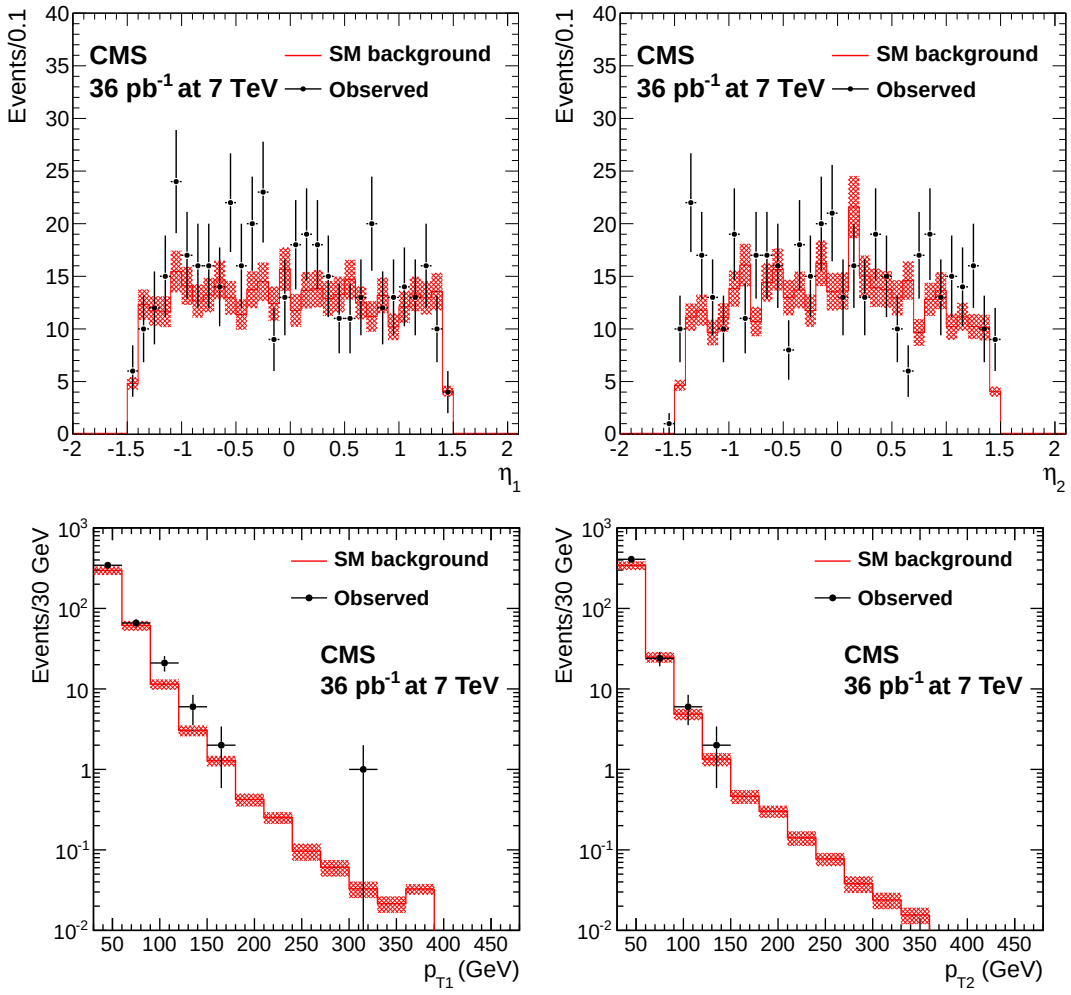


**Figure 5.2:** Distributions in $\eta$ and $E_T$ for the leading and sub-leading photons. Points with error bars represent data; the solid histogram corresponds to the expected background.

on the total background is calculated by adding individual background uncertainties in quadrature, except for those from the dijet and photon+jet backgrounds since they are both induced by the photon fake rate uncertainty. The relative combined background uncertainty is 21.8% which is dominated by the diphoton NLO K-factor uncertainty.

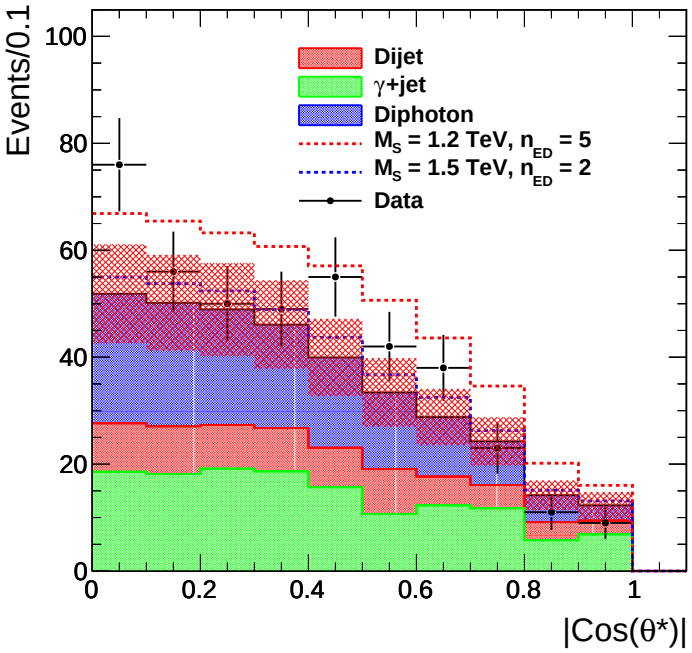


**Figure 5.3:** Scattering angle in c.o.m. frame of two photons

**Table 5.2:** Summary of systematic uncertainties.

| | Central Value | Relative Uncertainty |
|---|---|---|
| Luminosity | 36 pb $^{-1}$ | 4% |
| Background (Diphoton $K$ factor) | 0.30 Events | 23% |
| Signal Efficiency | 77.1% | 6.0% |
| Signal $K$ factor | 1.3 | 7.7% |

## 5.3 Limit setting method

The standard Bayesian approach is used in the limit setting [63]. Suppose that there is a set of parameters $(\sigma\lambda)$ involved in the experiment. $\sigma$ is the parameter of interest, for example cross section and $\lambda$ is a set of nuisance parameters, for example backgrounds, luminosity. The posterior density, $P(\sigma, \lambda|x)$, is related to the prior, $\pi(\sigma, \lambda)$, model, $P(\sigma, \lambda|x)$ densities by Bayes' theorem:

$$P(\sigma, \lambda|x) = \frac{P(x|\sigma, \lambda)\pi(\sigma, \lambda)}{\int\int P(x|\sigma, \lambda), \pi(\sigma, \lambda) d\lambda d\sigma} \tag{5.1}$$

x is the observable. The prior density in Eq. 5.1 can be factorized as:

$$\pi(\sigma, \lambda) = \pi(\lambda|\sigma)\pi(\sigma) \tag{5.2}$$

Usually, $\pi(\lambda|\sigma)$ is assumed as $\pi(\lambda)$. The integral over all of the spaces of the nuisance parameters is performed and the posterior density in Eq. 5.1 is now a normalized function of interested parameter $\sigma$. An upper limit, $\sigma^{CL}$, is found by:

$$CL = \int_0^{\sigma^{CL}} L(\sigma|x)d\sigma \tag{5.3}$$

In the counting experiment presented in this dissertation, the observable is the number of observed events, $n$ and the model density is conventional chosen as the Poisson likelihood of observing n events in data given a signal cross section times branching fraction times acceptance $S$, signal efficiency $\varepsilon$, the expected number of background events $B$, and an integrated luminosity $\mathcal{L}$:

$$P(n|S, \varepsilon, B, \mathcal{L}) = e^{-(B+\varepsilon S\mathcal{L})}\frac{(B + \varepsilon S\mathcal{L})^n}{n!}. \tag{5.4}$$

$S$ is the parameter of interest and the nuisance parameter set includes $\varepsilon$, $B$ and $\mathcal{L}$. A conventional flat prior is chosen for the cross section and the Lognormal functions with variance according to the uncertainties of the nuisance parameters are chosen as the priors of those. The 95% upper limit on the signal cross section is found by solving:

$$\int_0^{S^{95}(n)} L(n|S)dS = 0.95. \tag{5.5}$$

## 5.4 Limits on the Large Extra Dimension model

Using Table 5.2, the expected upper 95% CL limit on $S$ is 0.118 pb. This limit is translated to the limit on the parameters of the ADD model, by the following technique. Since the effects of virtual graviton exchange interfere with the SM diphoton production, generally, we expect the overall cross section of the diphoton production from physics sources to have the following form:

$$\sigma_{\mathrm{ADD}} = \sigma_{\mathrm{SM}} + \eta_G\, \sigma_{\mathrm{int}} + \eta_G^2\, \sigma_{\mathrm{ED}}, \tag{5.6}$$

where $\eta_G$ is the parameter specifying the strength of ED effects, as discussed in Section 1.5. Consequently, after subtracting the $\sigma_{\mathrm{SM}}$ term, the cross section is parametrized as a bilinear form in the parameter $\eta_G$. For $n_{\mathrm{ED}} = 2$ case, $\eta_G$ is not a constant, as it depends on the invariant mass of the diphoton pair. Therefore, in this case the signal cross section is parametrized with a smooth function of $1/M_S^4$. The limit on $1/M_S^4$ is found and further translated to the limit on the $M_S$. The

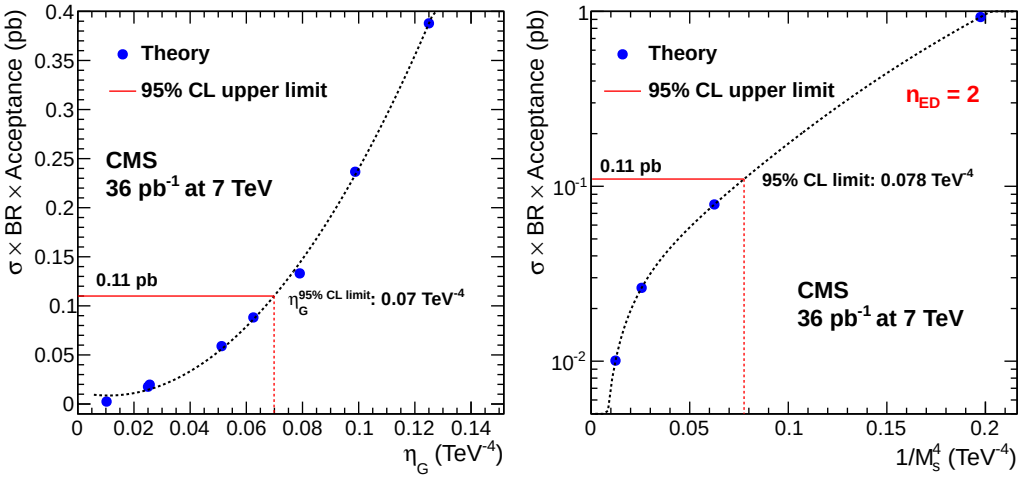


**Figure 5.4:** Signal cross section parameterization as a function of the strength of the LED, $\eta_G$ (left) and as a function of $1/M_s^4$ for the $n_{ED} = 2$ case (right).

expected 95% CL limit together with the signal cross section parametrization as a

function of $\eta_G$ are shown on the left in Figure 5.4. The intersection of the cross section limit with the signal cross section curve determines the upper 95% CL limit on the parameter $\eta_G$. As seen from the plot, these limits are equal to $\eta_G^{95} = 0.070$ TeV$^{-4}$ and $1/M_S^4(n = 2, 95\%) = 0.078$ TeV$^{-4}$. The translations to the lower limit on the fundamental Planck scale for various numbers of extra dimensions $n_{\rm ED}$ are trivially for $n_{\rm ED} = 2$ and for $n_{\rm ED} > 2$ by using Eq. (1.18). Table 5.3 shows those limits. The limits in convention [32] are identical for $n_{\rm ED} = 4$ HLZ limits; the limit in Hewett's convention with constructive interference is 1.73 TeV and is close to the HLZ limit for $n_{\rm ED} = 5$.

**Table 5.3:** Table of 95% CL limits on $M_S$ (in TeV), as a function of the convention and number of ED. A comparison of the limits with a truncation of the production cross section above $\sqrt{\hat{s}} > M_S$ is also shown.

| | HLZ | | | | | |
|---|---|---|---|---|---|---|
| | $n_{\rm ED} = 2$ | $n_{\rm ED} = 3$ | $n_{\rm ED} = 4$ | $n_{\rm ED} = 5$ | $n_{\rm ED} = 6$ | $n_{\rm ED} = 7$ |
| Full | 1.89 | 2.31 | 1.94 | 1.76 | 1.63 | 1.55 |
| Trunc. | 1.80 | 2.23 | 1.84 | 1.63 | 1.46 | 1.31 |
| | GWR | Hewett | | | | |
| | | Pos. | Neg. | | | |
| Full | 1.94 | 1.74 | 1.71 | | | |
| Trunc. | 1.84 | 1.60 | 1.50 | | | |

From the theory construction, the LO signal cross section calculations become non-perturbative when the $\hat{s}$ in the $2 \to 2$ process exceeds $M_S^2$. This effect is not taken into account in Sherpa cross section calculations used in this analysis, or in previous studies of this process at the Tevatron [64], where the effect is not expected to be important due to the lower machine energy. Since the energy of the LHC is significantly higher than the limits on $M_S$ which can be set in this analysis, it is necessarily to take into account this effect by conservatively assuming that the signal cross section is zero for $\sqrt{\hat{s}} > M_S$. Under these assumptions the limits on $M_S$ decrease by 5% for $n = 2$ (1.8 TeV) and 15% for $n = 7$ (1.31 TeV).

## 5.5 Conclusions

In conclusion, we have performed a search for large extra dimensions in the diphoton final state with a data sample collected in pp collisions at $\sqrt{s} = 7$ TeV corresponding to an integrated luminosity of 36 $pb^{-1}$. We optimize the signal selection to reach maximum sensitivity in a counting experiment in a one-sided mass window by selecting events with centrally produced photons ($|\eta| < 1.4442$) and large diphoton invariant mass ($m_{\gamma\gamma} > 500$ GeV). We estimate the SM backgrounds and compare with the observed data. Given the absence of an excess over the SM prediction, we set lower limits on the cutoff scale $M_S$ in the range 1.6-2.3 TeV. These results extend the current limits reached at the Tevatron in all but the $n_{ED} = 2$ case.

In addition to setting limits on a specific model of large extra dimensions, a model-independent limit on any new physics mode which results in central, high $p_T$ diphotons - either resonant or non-resonant (e.g. Kaluza-Klein gravitons in the Randall-Sundrum model [65]) is quoted. It is that a 95% C.L. exclusion on the cross section times branching fraction times acceptance of 118 fb is set for diphoton pairs with $M_{\gamma\gamma} > 500$ GeV and the following kinematic requirements on each of the two photons: $p_T > 30$ GeV and $|\eta| < 1.4442$.

While this analysis was being finalized, a phenomenological interpretation of the dijet angular distribution results from the CMS and ATLAS experiments appeared [66] and suggested even stronger limits on $M_S$. However, a dedicated experimental analysis and interpretation of the dijet data in the models with large extra dimensions has yet to be conducted.

# Bibliography


[1] W-M Yao. Review of particle physics. *J. Phys. G: Nucl. Part. Phys.*, 33, 2006.

[2] G. Landsberg. Collider searches for extra spatial dimensions and black holes. *e-print: arXiv:0808.1867*, 2008.

[3] The LHC study group. The Large Hadron Collider Conceptual Design. *CERN-AC-95-05*, 1995.

[4] W. L. Stirling R. K. Ellis and B. R. Webber. Qcd and collider physics. *Cambridge University Press*, 1996.

[5] J. Pumplin et al. New generation of parton distributions with uncertainties from global qcd analysis. *e-print arXiv:hep-ph/0201195*, 2002.

[6] N. Mondal A. Gupta and S. Raychaudhuri. Constraining large extra dimensions using dilepton data from the tevatron collider. *e-Print hep-ph/9904234*.

[7] D. J. Kapner et al. Tests of the gravitational inverse-square law below the dark-energy length scale. *Phys. Rev. Lett.*, 98, 2007.

[8] Lyndon Evans and Philip Bryant (editors). Lhc machine. *JINST*, S08001, 2008.

[9] The CMS Collaboration. Performance of the cms hadron calorimeter with cosmic ray muons and lhc beam data. *J. Instrum.*, 5:T03012, 2010.

[10] CMS Collaboration. Cms physics technical design report volume 1: Detector performance and software. *CERN-LHCC-2006-001*, 2006.

[11] The CMS collaboration. Tracking and primary vertex results in first 7 tev collisions. *CMS PAS TRK-10-005*, 2010.

[12] The CMS collaboration. Performance of muon reconstruction and identification in pp collisions at $\sqrt{s}$ =7 tev. *CMS PAS MUO-10-002*, 2010.

[13] CMS collaboration. Determination of the jet energy scale in cms with pp collisions at $sqrts = 7$ tev. *CMS PAS JME-10-010*, 2010.

[14] CMS collaboration. On measuring missing transverse energy with the cms detector in pp collisions at $\sqrt{s} = 7$ tev. *CMS PAPER JME-10-009*, 2010.

[15] The CMS Collaboration. Photon reconstruction and identification at $\sqrt{s} = 7$ tev. *CMS PAS EGM-10-005*, 2010.

[16] The CMS Collaboration. Electron reconstruction and identification at $\sqrt{s} = 7tev$. *CMS PAS EGM-10-004*, 2010.

[17] The CMS collaboration. Electromagnetic calorimeter commissioning and first results with 7 tev data. *CMS Note 2010/012*, 2010.

[18] Sheldon L. Glashow. Partial-symmetries of weak interactions. *Nucl. Phys.*, 22, 1961.

[19] S. Weinberg. A model of leptons. *Phys. Rev. Lett.*, 19, 1967.

[20] A Salam. Elementary particle physics: Relativistic groups and analyticity. *N. Svartholm (Almqvist & Wiksell)*, 1968.

[21] G. 't Hooft. Renormalization of massless yang-mills fields. *Nucl. Phys.*, 33, 1971.

[22] D. J. Gross and F. Wilczek. Ultraviolet behavior of non-abelian gauge theories. *Phys. Rev. Lett.*, 30, 1973.

[23] H. D. Politzer. Reliable perturbative results for strong interactions? *Phys. Rev. Lett.*, 30, 1973.

[24] F. Abe et al. Observation of top quark production in $p\overline{p}$ collisions with the collider detector at fermilab. *Phys. Rev. Lett.*, 74, 1995.

[25] S. Abachi et al. Observation of the top quark. *Phys. Rev. Lett.*, 74, 1995.

[26] K. Kodama et al. Observation of tau neutrino interactions. *Phys. Lett. B*, 504, 2001.

[27] Nakamura et al. (Particle Data Group). Review of Particle Physics, 2010-2011. Review of Particle Properties, 2010-2011. *J. Phys. G*, 37, 2010.

[28] D. E. Soper J. C. Collins and G. Sterman. Factorization of hard processes in qcd. *e-print arXiv:hep-ph/0409313*, 2004.

[29] N. Arkani-Hamed, S. Dimopoulos, and G. Dvali. The hierarchy problem and new dimensions at a millimeter. *Phys. Lett. B*, 429:263, 1998.

[30] J.C. Long and J.C. Price. *e-print arXiv:hep-ph/0303057v2*, 2003.

[31] G. Landsberg. Collider searches for extra dimensions. *Preprint hep-ex/0412028*, 2004.

[32] R. Rattazzi G. Giudice and J. Wells. Quantum gravity and extra dimensions at high-energy colliders. *Nucl. Phys.*, B544:3, 1999.

[33] J. Hewett. Indirect collider signals for extra dimensions. *Phys. Rev. Lett.*, 82:4765, 1999.

[34] J. Lykken T. Han and R. Zhang. On kaluza-klein states from large extra dimensions. *Phys. Rev. D*, 59:105006, 1999.

[35] E. G. Adelberger. Sub-mm tests of the gravitational inverse-square law. *e-Print hep-ex/0202008*, 2002.

[36] S. Cullen and M. Perelstein. *Phys. Rev. Lett.*, 83, 1999.

[37] CMS collaboration. The cms experiment at the cern lhc. *JINST 3*, S08006, 2008.

[38] CMS Collaboration. Electromagnetic calorimeter calibration with 7 tev data. *CMS PAS EGM-10-003*, 2010.

[39] CMS Collaboration. Cms the tridas project technical design report, volume 1: The trigger systems. *CERN/LHCC 2000-38*, 2000.

[40] The CMS collaboration. Track reconstruction in the cms tracker. *CMS PAS TRK-09-001*, 2009.

[41] R. Fruhwirthu. Application of kalman filtering to track and vertex fitting. *Nucl. Instrum. Meth.*, A262, 1987.

[42] Tracking and b Tagging POGs. Tracking and vertexing results from first collisions. *CMS AN-2010/055*, 2010.

[43] R. Fruewirth et al. Adaptive vertex fitting. *CMS Note 2007/008*, 2007.

[44] CMS collaboration. Performance of jet algorithms in cms. *CMS PAS JME-07-003*, 2007.

[45] G. C. Blazey et al. Run ii jet physics: Proceedings of the run ii qcd and weak boson physics workshop. *hep-ex 0005012*, 2000.

[46] M. Cacciari et al. The anti-kt jet clustering algorithm. *JHEP*, 0804:063, 2008.

[47] CMS collaboration. Jet plus tracks algorithm for calorimeter jet energy corrections in cms. *CMS PAS JME-09-002*, 2009.

[48] CMS collaboration. Particle-flow event reconstruction in cms and performance for jets, taus, and $e_T^m iss$. *CMS PAS PFT-09-001*, 2009.

[49] CMS collaboration. Commissioning of trackjets in pp collisions at $\sqrt{s} = 7$ tev. *CMS PAS JME-10-006*, 2010.

[50] The CMS collaboration. Jet performance in pp collisions at $\sqrt{s} = 7$ tev. *CMS PAS JME-10-003*, 2010.

[51] S. Esen et al. Missing transverse energy performance in cms. *CMS AN-2007/041*, 2007.

[52] CMS collaboration. Performance of missing transverse energy using calorimeter and tracks in cms. *CMS PAS JME-09-006*, 2009.

[53] C. Seez E. Meschi, T. Monteiro and P. Vikas. Electron reconstruction in the cms electromagnetic calorimeter. *CMS Note 2001/034*, 2001.

[54] N. Marinelli. Track finding and identification of converted photons. *CMS NOTE 2006/005*, 2006.

[55] W. Adam et al. Electron reconstruction in cms. *CMS AN-2009/164*, 2009.

[56] W. Adam et al. Reconstruction of electrons with the gaussian-sum filter in the cms tracker at the lhc. *CMS NOTE 2005/001*, 2005.

[57] S. Mrenna T. Sjostrand and P. Skands. Pythia 6.4 physics and manual. *JHEP*, 05, 2006.

[58] S. Mrenna T. Sjostrand and P. Skands. A brief introduction to pythia 8.1. *arXiv:0710.3820*.

[59] K. Matchev A. Schalicke S. Schumann G. Soff T. Gleisberg, F. Krauss. Helicity formalism for spin-2 particles. *e-print: arXiv:hep-ph/0306182*, 2003.

[60] Matteo Sani. Photon efficiency measurements using tag and probe. *CMS AN-2010/292*, 2010.

[61] A. Askew et al. A first search for general gauge mediated susy. *CMS Note*, 2010.

[62] T. Binoth et al. A full next-to-leading order study of direct photon pair production in hadronic collisions. *Eur. Phys. J.*, 2000.

[63] I. Bertram et al. A recipe for the construction of confidence limits. *FERMILAB-TM-2104*, 2000.

[64] D0 collaboration. Search for large extra spatial dimensions in the dielectron and diphoton channels in $p\overline{p}$ collisions at $\sqrt{s} = 1.96$ tev. *Phys. Rev. Lett.*, 102, 2009.

[65] R. Sundrum L. Randall. *Phys. Rev. Lett.*, 83:3370 and ibid (1999) 4690, 1999.

[66] P. Giardino et al. R. Franceschini, G. Giudice. Lhc bounds on large extra dimensions. *e-print: arXiv:1101.4919*, 2011.